Nano Research

ISSN 1998-0124 CN 11-5974/O4
https://doi.org/10.26599/NR.2026.94909275

Research Article

Cobalt doping-induced spin polarization and *in-situ* Bi^0 decoration of Bi_2MoO_6 synergistically boosting photocatalytic CO_2-to-CO conversion

Yanyan Dai[1,2], Qianfei Ma[3], Xiaofeng Sun[4], Zainab Mehfooz[5], Zao Yi[6], Jinyuan Ma[1], Huaijing Chen[2], Guorong Liu[2], Zhansheng Lu[3], Hua Yang[1,2](✉)

[1] State Key Laboratory of Advanced Processing and Recycling of Non-ferrous Metals, Lanzhou University of Technology, Lanzhou 730050, China

[2] School of Science, Lanzhou University of Technology, Lanzhou 730050, China

[3] College of Mathematics and Physics, Bejing University of Chemical Technology, Beijing 100029, China

[4] School of Electronic Information Engineering, Lanzhou institute of technology, Lanzhou 730050, China

[5] Institute of Physics, The Islamia University of Bahawalpur, Punjab, Pakistan

[6] School of Chemistry and Chemical Engineering, Jishou University, Jishou 416000, China

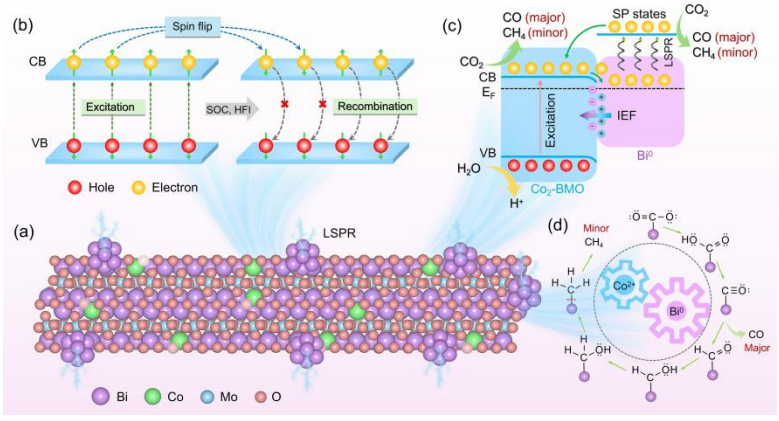
Nano Res., **Just Accepted Manuscript** • https://doi.org/10.26599/NR.2026.94909275

https://www.sciopen.com/journal/1998-0124 on Oct. 20, 2026

© The Authors(s)

Just Accepted

This is a "Just Accepted" manuscript, which has been examined by the peer-review process and has been accepted for publication. A "Just Accepted" manuscript is published online shortly after its acceptance,which is prior to technical editing and formatting and author proofing. Tsinghua University Press (TUP) provides "Just Accepted" as an optional and free service which allows authors to make their results available to the research community as soon as possible after acceptance. After a manuscript has been technically edited and formatted, and the page proofs have been corrected, it will be removed from the "Just Accepted" web site and published officially with volume and article number (e.g., *Nano Research*, **2025**, *18*, 94906990). Please note that technical editing may introduce minor changes to the manuscript text and/or graphics which may affect the content, and all legal disclaimers that apply to the journal pertain. In no event shall TUP be held responsible for errors or consequences arising from the use of any information contained in these "Just Accepted" manuscripts. To cite this anuscript please use its Digital Object Identifier (DOI®),which is identical for all formats of publication.



This study develops Co-doped and surface Bi^0 nanocrystal-modified BMO photocatalysts through a facile one-step solvothermal method, achieving the synergistic integration of multiple factors (including Co doping induced spin polarization, Bi^0/Co-BMO interfacial charge transfer and LSPR of Bi^0 nanocrystals) to boost CO_2 photoreduction performance.

Just Accepted

Research Article

Cobalt doping-induced spin polarization and *in-situ* Bi^0 decoration of Bi_2MoO_6 synergistically boosting photocatalytic CO_2-to-CO conversion

Yanyan Dai[1,2], Qianfei Ma[3], Xiaofeng Sun[4], Zainab Mehfooz[5], Zao Yi[6], Jinyuan Ma[1], Huaijing Chen[2], Guorong Liu[2], Zhansheng Lu[3], Hua Yang[1,2,*]

[1]State Key Laboratory of Advanced Processing and Recycling of Non-ferrous Metals, Lanzhou University of Technology, Lanzhou 730050, China

[2]School of Science, Lanzhou University of Technology, Lanzhou 730050, China

[3]College of Mathematics and Physics, Bejing University of Chemical Technology, Beijing 100029, China

[4]School of Electronic Information Engineering, Lanzhou institute of technology, Lanzhou 730050, China

[5]Institute of Physics, The Islamia University of Bahawalpur, Punjab, Pakistan

[6]School of Chemistry and Chemical Engineering, Jishou University, Jishou 416000, China

Received: 15 September 2026; **Revised:** 8 October 2026; **Accepted:** 20 October 2026

*Address correspondence to hyang@lut.edu.cn

Cite this article: *Nano Research*, 2026, 19, 94909275

https://doi.org/10.26599/NR.2026.94909275

Abstract: Photocatalytic CO_2 reduction utilizing solar energy to convert CO_2 into value-added fuels and chemicals is regarded as a promising strategy for alleviating energy crises and achieving carbon cycling. However, this process remains limited by rapid recombination of photogenerated carriers and sluggish CO_2 activation kinetics. In this work, Bi_2MoO_6

Just Accepted

(BMO)-based photocatalysts with Co doping and in-situ formation of Bi^0 nanocrystals were developed through a facile one-step solvothermal method. X-ray absorption spectroscopy analysis reveals that Co species are atomically dispersed within the BMO lattice in a CoO_4 coordination configuration. The weak crystal-field environment of CoO_4 preserves unpaired 3d electrons and induces spin-polarized electronic states, thereby decreasing the photocarrier recombination. Meanwhile, the Co doping leads to in-situ formation of Bi^0 nanocystals on the catalyst surface, which promotes photocarrier transfer between Bi^0 and Co-BMO and facilitates the photocarrier separation. The Co doping increases the CO_2 adsorption energy on the Bi active sites and decreases the energy barrier for the formation of the key *COOH intermediate. Moreover, the Co doping generates extra Co and Bi^0 active sites for CO_2 photoreduction reactions. The cascade synergistic mechanism significantly boosts the photocatalytic CO_2-to-CO conversion, where the optimal Co_2-BMO sample delivers a CO production rate of 158.47 μmol g^{-1} h^{-1} that is 3.8 times higher than that of pristine BMO. This work provides an intriguing strategy for designing efficient solar-driven CO_2 conversion photocatalysts from the perspectives of electronic spin manipulation and interfacial charge transfer.

Keywords: cobalt-doped Bi_2MoO_6; spin polarization; Bi^0 nanocrystal decoration; photocatalytic CO_2 reduction; cascade synergistic mechanism

Just Accepted

1. Introduction

Sustained excessive consumption of fossil fuels has caused severe energy crises and global climate challenges. The photocatalytic CO_2 reduction reaction, which utilizes solar energy to convert CO_2 into high-value-added chemicals and fuels, is regarded as a green and sustainable strategy for carbon neutrality [1–4]. Nevertheless, there are multiple factors impeding the reaction efficiency, such as sluggish kinetics of photogenerated charge carriers, rapid photocarrier

recombination, and weak CO_2 adsorption and activation capability on catalyst surfaces [5–7]. Overcoming these barriers is crucial for achieving highly efficient photocatalytic CO_2 reduction.

Aurivillius-phase oxide Bi_2MoO_6 (BMO) has attracted extensive attention in photocatalytic CO_2 reduction due to its unique layered crystal structure, suitable band-edge positions and excellent chemical stability [8,9]. However, pristine BMO still suffers from inherent drawbacks, including severe photocarrier recombination, sluggish photocarrier migration kinetics and insufficient CO_2 adsorption and activation capability, which severely restrict its practical photocatalytic applications [10]. To overcome these limitations, various strategies, such as morphology engineering, heterojunction construction, elemental doping, defect engineering and cocatalyst loading, have been developed to regulate the structural and electronic properties of BMO [11–14]. These approaches have made progress in enhancing photocatalytic CO_2 reduction. Among them, constructing heterojunctions is an important method for promoting photocarrier separation [15,16]. However, the heterojunction formation depends highly on the energy band alignment as well as the interfacial interaction, increasing the difficulty of precisely regulating the photocarrier transfer and separation.

In recent years, electron spin has emerged as an important additional degree of freedom in modifying photocatalytic systems [17–20]. Unlike heterojunction regulation approach, which relies on energy band alignment and interfacial interaction, spin polarization can regulate carrier migration and recombination kinetics by modifying the electronic spin-state distribution [21]. Previous studies have demonstrated that introducing magnetic ions with unpaired electrons (such as Fe, Co, Ni and Mn) can induce spin-asymmetric electronic structures in nonmagnetic semiconductors, thereby modulating the spin-state distribution of photocarriers to promote their separation and optimize reaction dynamics [22–27]. For instance, Co-doped BiOCl system has been reported to utilize spin-polarized electronic states to enhance photocarrier separation and promote CO_2 reduction processes [26]. Similarly, the incorporation of Ni^{2+} into $BaTiO_3$ thin films

Just Accepted

was also shown to be capable of enhancing photocarrier separation through spin-related effects [27]. These studies demonstrate that spin regulation provides a new avenue for overcoming photocarrier kinetic limitations in photocatalytic systems. However, current spin polarization strategies mainly focus on modulating bulk electronic structures, while the synergistic regulation of spin polarization and surface/interface charge behavior remains insufficiently explored.

Metal nanoparticles have demonstrated to be important cocatalysts for boosting the photocatalytic conversion of CO_2 into renewable carbonaceous fuels [28–30]. Notably, metal nanoparticles are highlighted due to their plentiful surface active sites and remarkable local surface plasmon resonance (LSPR) effect [31–33]. The LSPR effect of metal nanoparticles can not only promote the photocarrier generation and separation, but also promote the excitation of electrons into surface plasmon (SP) states with higher reduction potential [33]. Moreover, the decoration of metal nanoparticles onto photocatalysts can establish an interfacial electric field (IEF) through interfacial charge redistribution, promoting the transfer of photoelectrons and decreasing their recombination with photoholes. For example, Zhao et al. reported a $Bi@Bi_2MoO_6$ photocatalyst in which metallic Bi nanoparticles were deposited on Bi_2MoO_6 nanosheets. The introduction of Bi nanoparticles enhanced photocatalytic CO_2 reduction performance, which was attributed to improved charge separation and the LSPR effect of metallic Bi [34]. It is noted that compared with external loading of metal cocatalysts, in-situ generation of cocatalysts onto photocatalysts can establish a strong interfacial interaction that is beneficial to interfacial charge migration. For example, Li et al. employed a nonequilibrium solvothermal strategy to induce the in-situ exsolution of Bi^0 nanoparticles from the $Bi_4Ti_3O_{12}$ lattice, constructing a tightly coupled $Bi^0/Bi_4Ti_3O_{12}$ heterointerface that efficiently drives interfacial charge migration/separation and optimizes CO_2 adsorption and activation processes [35]. It is expected that the simultaneous adoption of electron spin regulation and metal nanoparticle modification will afford a great potential to synergistically manipulate the electronic structures of

Just Accepted

photocatalysts and charge dynamics, thus achieving highly efficient CO_2 photoreduction performance.

Based on the above considerations, herein we introduce cobalt element in BMO through a facile one-step solvothermal process to achieve partial substitution of Bi^{3+} species by Co species and simultaneously in-situ formation of Bi^0 nanocrystals on the catalyst surface. Experimental characterizations and theoretical calculations reveal that Co species are atomically dispersed within the BMO lattice in a CoO_4 local coordination configuration, inducing spin-polarized electronic states. Meanwhile, the displaced Bi^{3+} species are reduced into Bi^0 nanocrystals on the catalyst surface to form Bi^0/Co-BMO heterojunctions. The Co doping induced spin polarization, Bi^0/Co-BMO interfacial electric field and LSPR effect of Bi^0 nanocrystals synergistically promote photogenerated carrier separation and migration as well as enhance CO_2 adsorption and activation. As a result, the Co-doped BMO systems exhibit enhanced photocatalytic CO_2-to-CO conversion compared with pristine BMO. The optimal Co_2-BMO photocatalyst achieves a CO production rate of 158.47 μmol g^{-1} h^{-1}, which is 3.8 times higher than that of pristine BMO. This work provides an important strategy for designing highly efficient photocatalytic systems in CO_2 photoreduction application through the coordinated manipulation of electronic spin states and interfacial charge transfer.

2. Experimental

2.1. Preparation of BMO

Hierarchical flower-like BMO microspheres were synthesized using a solvothermal method. Typically, 2 mmol of $Bi(NO_3)_3 \cdot 5H_2O$ and 1 mmol of $Na_2MoO_4 \cdot 2H_2O$ were separately dissolved in 10 mL of ethylene glycol (EG). After magnetic stirring for 30 min, both solutions were slowly added dropwise into 40 mL of ethanol. Following continuous stirring for 60 min, the mixture was transferred into an autoclave with a capacity of 100 mL, sealed and reacted at 160 °C for 24 h. The precipitate generated through the solvothermal reaction was collected by centrifugation,

Just Accepted

washed several times with deionized water and ethanol to remove residual impurities, and finally dried at 60 °C for 8 h. The product was obtained as hierarchical flower-like BMO microspheres.

2.2. Preparation of Co-BMO

Co-doped BMO samples were prepared using the same solvothermal method. Specifically, 2 mmol of $Bi(NO_3)_3 \cdot 5H_2O$ and a stoichiometric amount of $Co(NO_3)_2 \cdot 6H_2O$ (0.02, 0.1 or 0.2 mmol) were dissolved in 10 mL of EG. Separately, 1 mmol of $Na_2MoO_4 \cdot 2H_2O$ was dissolved in another 10 mL of EG. After magnetic stirring for 30 min, both solutions were slowly added dropwise into 40 mL of ethanol. Following continuous stirring for 60 min, the mixture was reacted in a 100 mL autoclave at 160 °C for 24 h. After completion of the reaction, the precipitate was washed and dried to obtain Co-doped BMO samples. The samples synthesized by introducing 0.02, 0.1 and 0.2 mmol of $Co(NO_3)_2 \cdot 6H_2O$ were denoted as Co_1-BMO, Co_2-BMO and Co_3-BMO, respectively.

2.3. Characterization and DFT calculation methods

The prepared photocatalysts were systematically characterized using various techniques to investigate their structures, morphologies, chemical environments and electronic properties, including X-ray powder diffraction (XRD), scanning/transmission electron microscopy (SEM/TEM), X-ray photoelectron spectroscopy (XPS), Fourier transform infrared (FT-IR) spectroscopy, synchrotron X-ray absorption spectroscopy (XAS), ultraviolet–visible diffuse reflectance spectroscopy (UV–vis DRS), steady-state photoluminescence (PL) spectroscopy, vibrating sample magnetometry (VSM), and femtosecond transient absorption (fs-TA) spectroscopy. Electrochemical measurements were performed using a three-electrode configuration. First-principles density functional theory (DFT) calculations were carried out using the Vienna Ab initio Simulation Package (VASP) [36]. Detailed characterization procedures, electrochemical measurement protocols, DFT computational parameters and related instruments information are provided in the Supplementary Material.

2.4. Photocatalytic CO_2 reduction measurements

Just Accepted

The photocatalytic activities of as-fabricated photocatalysts for CO_2 reduction were measured using a Labsolar-6A fully automatic all-glass online trace gas analysis system (Beijing Perfectlight Technology Co., Ltd., China). The generated intermediates during the CO_2 reduction reactions were probed by in-situ diffuse reflectance infrared Fourier transform spectroscopy (DRIFTS) on a Nicolet iS50 FTIR spectrometer with an MCT detector. Further details on the CO_2 photoreduction and in-situ DRIFTS testing procedures and parameters can be found in the Supplementary Material.

3. Results and discussion

3.1. Basic characterization of photocatalysts

Fig. 1(a) illustrates the synthesis process of BMO and Co-BMO hierarchical microspheres, together with their corresponding crystal structure schematics. The crystal structures of the as-prepared samples were characterized by means of XRD. As shown in Fig. 1(b), all the diffraction peaks of the pristine BMO sample can be perfectly indexed according to the orthorhombic BMO phase (PDF#84-0787, space group $Pca2_1$). The lattice parameters of pristine BMO are determined to be a = 5.5312 Å, b = 16.2266 Å and c = 5.5142 Å according to the Rietveld refinement (Fig. S1). With the introducing Co element, extra diffraction peaks assignable to metallic Bi^0 (PDF#05-0519) are detectable, and the intensity of the Bi^0 peaks increases with increasing Co content. The diffraction peak widths and positions of BMO show no noticeable changes upon Co doping, as seen from the enlarged XRD patterns in Fig. 1(c). The XRD results manifest that Co species partially substitute Bi sites in the BMO lattice, and the Co substitution induces local charge compensation and electronic structure reconstruction, which promotes the reduction of partial Bi^{3+} species into Bi^0 nanocrystals that are distributed on the material surface [37].

The preferential occupation behavior of Co in the BMO lattice was investigated by calculating the substitution formation energy within the DFT framework. The formation energies

Just Accepted

for Co substitution at the Bi1, Bi2 and Mo sites were calculated, according to the following equation: $E_{formation} = E(defect) - E(perfect) + E(Bi/Mo) - E(Co)$ [38], to be 2.80, 2.74 and 8.29 eV, respectively, as demonstrated in Fig. S2 and Table S1. Compared with Mo-site substitution, Co incorporation at Bi sites requires much lower formation energy, indicating that Co preferentially occupies Bi sites in the BMO lattice from a thermodynamic perspective. The comparable formation energies between the Bi1 and Bi2 sites suggest that both Bi sites are favorable for Co substitution. It is noted that Co species has a smaller ionic radius than the Bi species, indicating that the Co substitution for Bi could induce the lattice shrinkage. However, the XRD result shows almost no lattice change upon the Co doping. This is because oxygen vacancies are simultaneously introduced into the lattice upon Co doping as evidenced by the next XPS analysis, and the introduction of oxygen vacancies is expected to cause the lattice expansion [39] and offset the lattice shrinkage induced by the Co substitution. To verify the existence and distribution of Bi^0, the Co_2-BMO sample was treated with 0.05 M dilute nitric acid. It is found that after acid treatment, the Bi^0 diffraction peaks completely disappear, while the characteristic diffraction peaks of Co_{doped}-BMO remain unchanged (Fig. S3). The easy dissolution and elimination of Bi^0 by dilute nitric acid suggest that the generated Bi^0 nanocrystals are mainly distributed on the Co_{doped}-BMO surface or near-surface regions.

The FT-IR spectra of BMO and Co_2-BMO were measured to further reveal the structural information of the samples, as displayed in Fig. S4. The characteristic peaks located at 448 and 571 cm^{-1} are respectively assigned to the stretching and bending vibrations of Bi–O bonds, while the absorption bands at 734 and 841 cm^{-1} correspond to the asymmetric and symmetric stretching vibrations of Mo–O bonds in the MoO_6 octahedra [40,41]. Notably, the shapes of the characteristic absorption peaks of the Co_2-BMO sample are very similar to those of pristine BMO, but their intensities decrease noticeably. This phenomenon indicates that the Co doping does not disrupt the intrinsic BMO lattice structure, while the local coordination environment within the

Just Accepted

lattice framework could be modified [42]. In addition, extra absorption peaks are observed for the samples, among which the peaks at 1050/1084/1115 cm^{-1} are associated with C–O vibrations, the peak at 1384 cm^{-1} is related to CO_3^{2-} vibration, and the peak at 1632 cm^{-1} is attributed to O–H vibration of water molecules [43,44]. The CO_3^{2-} group and water molecules are generally observed on the FT-IR spectra and could stem from airborne contaminants during the measurement process.

XPS measurements were performed on BMO and Co_2-BMO to elucidate the binding energies and chemical states of the elements, and the acquired high-resolution Co 2p, O 1s, Bi 4f and Mo 3d core-level XPS spectra are presented in Fig. 1(d)–(g), respectively. The Co 2p spectrum of Co_2-BMO (Fig. 1(d)) presents the characteristic signals of Co $2p_{3/2}$ (781.5 eV) and Co $2p_{1/2}$ (796.9 eV) although their intensity are very weak, indicating the doping of Co species in the BMO lattice [45]. The O 1s spectra (Fig. 1(e)) can be deconvoluted into lattice oxygen (O_L), chemisorbed oxygen (O_{ads}) and surface hydroxyl species (–OH)/water molecules [46–48]. Generally, chemisorbed oxygen is associated with the formation of oxygen vacancies. Compared with pristine BMO, the O_{ads} component in Co_2-BMO is significantly enhanced, suggesting the generation of oxygen vacancies induced by the Co doping, which may originate from the local charge compensation process associated with the Co incorporation [49]. In the Bi 4f spectra in Fig. 1(f), the two strong peaks are assigned to the Bi $4f_{7/2}$ and $4f_{5/2}$ signals of Bi^{3+} species [46,47]. Besides the strong peaks related to Bi^{3+} species, the Co_2-BMO sample displays an additional pair of weak peaks at 157.6 and 163.1 eV, which can be assigned to Bi^0 species [50]. This result is consistent with the XRD analysis, further suggesting that the Co doping replaces partial lattice Bi^{3+} species and results in the formation of Bi^0 nanocrystals on the catalyst surface. The Mo 3d spectra of both BMO and Co_2-BMO samples (Fig. 1(g)) show two characteristic peaks separately corresponding to the Mo $3d_{5/2}$ and $3d_{3/2}$ binding energies of Mo^{6+} species [46,47]. No extra oxidation states of Mo are detectable upon the Co doping. Additionally, the Bi 4f and Mo 3d

Just Accepted

peaks of Co_2-BMO exhibit a slight positive shift in binding energy, indicating that the Co doping and Bi^0 nanocrystal construction jointly regulate the local electronic environment of BMO [51].

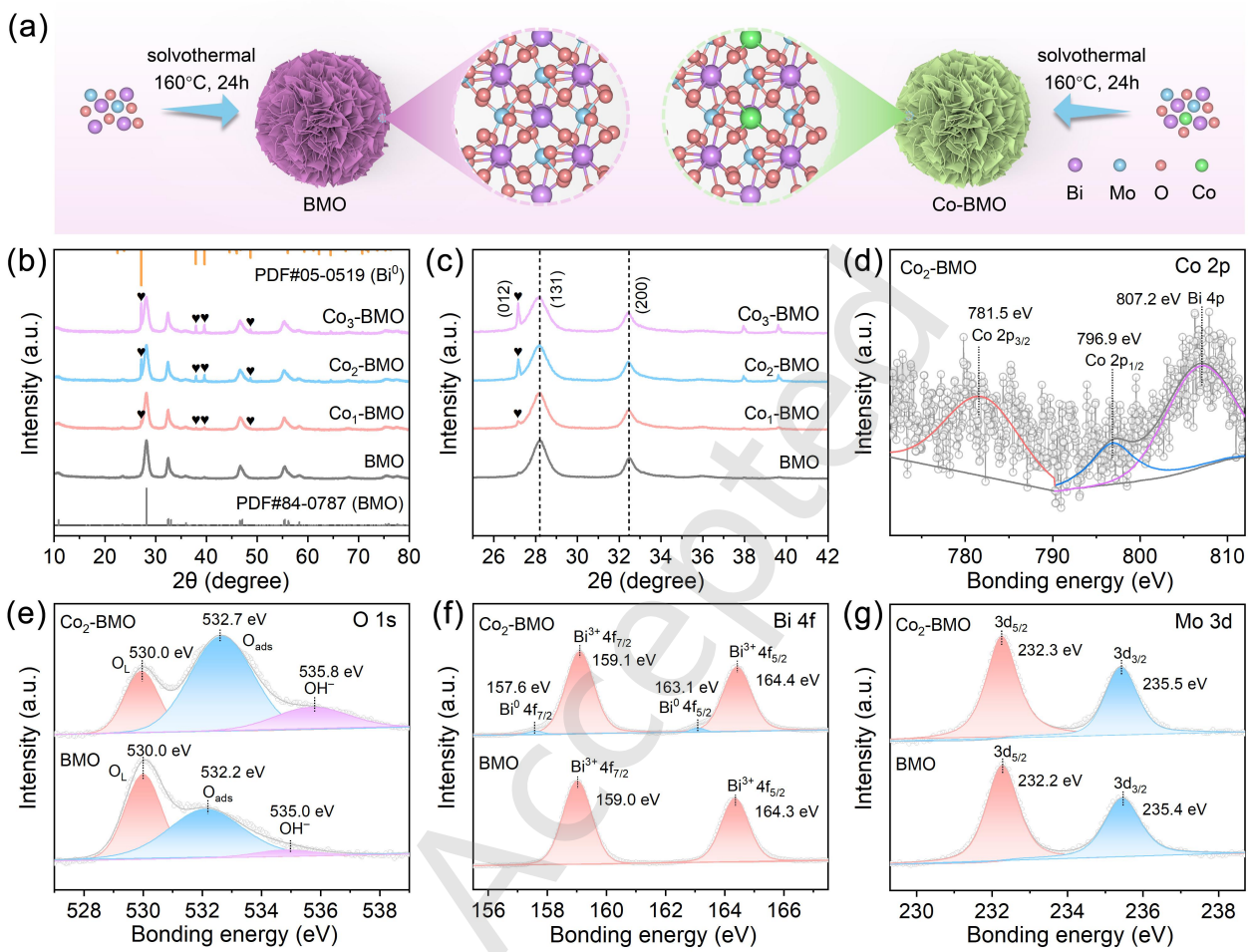


Fig. 1. (a) Schematic diagram illustrating the preparation of flower-like BMO and Co-BMO hierarchical microspheres; (b) XRD patterns of BMO and Co-doped BMO samples and (c) local magnified XRD patterns; XPS spectra of (d) Co 2p, (e) O 1s, (f) Bi 4f and (g) Mo 3d.

SEM and TEM techniques were combined to examine the morphology and microstructure of BMO and Co_2-BMO. The SEM images of BMO (Fig. 2(a)) and Co_2-BMO (Fig. 2(b)) show that both samples are composed of flower-like hierarchical microspheres with a diameter of 1–2 μm, and the hierarchical microspheres are self-assembled from small-sized nanoflakes. The Co doping does not cause changes in the morphology and microstructure of the photocatalysts. The TEM image of Co_2-BMO (Fig. 2(c)) more clearly depicts the morphological feature of flower-like

Just Accepted

hierarchical architectures assembled from nanoflakes. Small-sized nanoparticles of several nanometers in diameter, determined to be Bi^0 nanocrystals, are seen to be decorated on the surface of Co-BMO nanoflakes. The acquired selected area electron diffraction (SAED) pattern in Fig. 2(d) presents several concentric polycrystalline diffraction rings, among which the brightest and relatively wide ring can be attributed to the overlapping of Co-BMO (131) and Bi^0 (012) diffraction rings. The SAED pattern confirms the formation of a well-definite orthorhombic phase of Co-BMO with decoration of Bi^0 nanocrystals. The high-resolution TEM (HRTEM) image in Fig. 2(e) clearly shows two types of lattice structures, which are separately assigned to Co-BMO (d_{111} = 0.378 nm) and Bi^0 (d_{101} = 0.374 nm) through precise lattice spacing measurement (Fig. 2(f)). The elemental mapping analysis, as shown in Fig. 2(g–k), reveals that besides the Bi, Mo and O elements, Co signal is also uniformly detected throughout the entire hierarchical microsphere, supporting the successful incorporation of Co into BMO from a chemical composition perspective. The element contents of the Co-BMO samples were measured through inductively coupled plasma-mass spectrometry (ICP-MS) and are presented in Table S2, revealing that the Co contents in the samples are close to the stoichiometric values.

Just Accepted

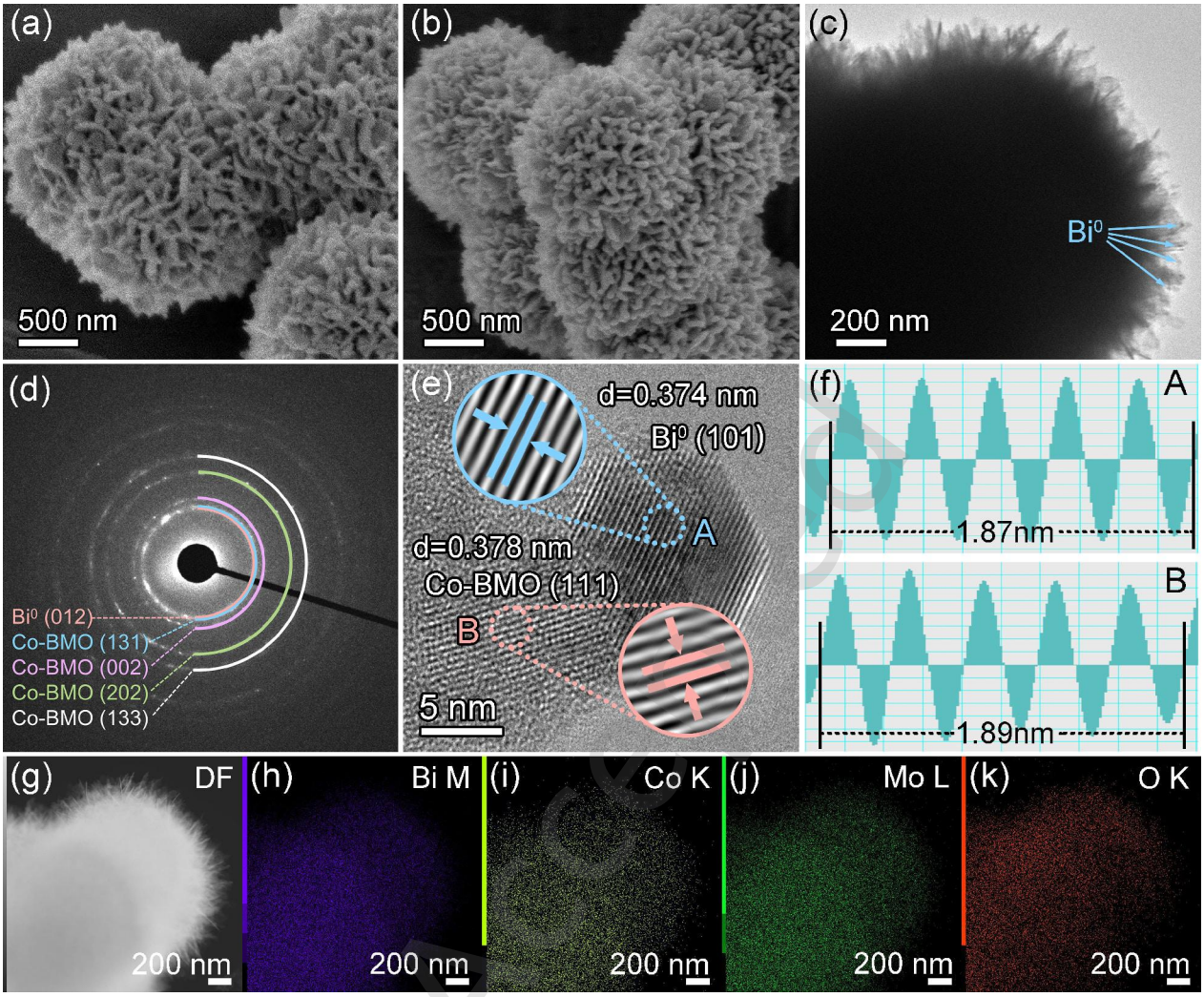


Fig. 2. SEM images of (a) BMO and (b) Co_2-BMO; (c) TEM image, (d) SAED pattern, (e) HRTEM image, (f) lattice spacing profile image of the select area in e, (g) high-angle annular dark-field TEM image and (h–k) elemental mapping images of Co_2-BMO.

The aforementioned analysis indicates that Co is preferentially doped at the Bi sites of BMO. To further elucidate the doping mechanism and local coordination environment of Co, X-ray absorption fine structure (XAFS) analyses were carried out. Co K-edge XAFS measurements were performed on Co_2-BMO and the reference samples. Among them, Co foil, CoO and Co_3O_4 were used as references for Co species with different oxidation states, while CoPc served as a model of a typical four-coordinated Co center to assist in identifying the local coordination structure of Co. As shown in Fig. 3(a), the absorption edge position and white-line intensity of

Just Accepted

Co_2-BMO are higher than those of Co foil and are very close to those of CoO, indicating that Co mainly exists in an oxidized state with an average valence state close to +2. In addition, a distinct pre-edge peak is observed at approximately 7710 eV, which can be attributed to the Co 1s → 3d electronic transition. Its characteristics are closely related to the hybridization between the Co 3d orbitals and the O 2p orbitals of the coordinating oxygen atoms, suggesting strong electronic interactions between the Co center and the surrounding oxygen coordination environment [52,53].

To further elucidate the local coordination structure of Co, k^2-weighted extended X-ray absorption fine structure (EXAFS) spectra were Fourier transformed into *R* space for analysis. As shown in Fig. 3(b), Co_2-BMO exhibits only a distinct Co–O scattering feature at approximately 1.46 Å, while no typical Co–Co or Co–O–Co scattering peaks associated with Co foil and cobalt oxide references are observed. This result suggests that Co species do not form metallic particles or cobalt oxide clusters, but instead exist in an atomically dispersed state within the BMO framework. Further analysis of the k^2-weighted EXAFS oscillation curves (Fig. 3(c)) reveals that Co_2-BMO exhibits distinct oscillation characteristics compared with those other reference samples, further confirming its unique local coordination environment.

Co K-edge wavelet transform analysis was further performed to verify the local coordination environment of Co species. As shown in Fig. 3(d), Co_2-BMO exhibits only an intensity distribution corresponding to Co–O scattering, without any high-*k* region signals associated with Co–Co or Co–O–Co scattering pathways. In contrast, Co foil shows a distinct Co–Co scattering feature, while CoO or Co_3O_4 exhibits distinct Co–O–Co scattering features. This result further excludes the formation of metallic cobalt or cobalt oxide clusters. Combined with the EXAFS fitting results (Fig. 3(e–g), Fig. S5 and Table S3), the average coordination number of the central Co atom is determined to be approximately 4.12, which is close to the typical four-coordinated Co-N_4 structure in CoPc, indicating that Co exists in a four-coordinated configuration within the

Just Accepted

BMO lattice [54]. Considering that only the Co–O scattering pathway is identified from the EXAFS analysis, this four-coordinated structure can be assigned to a CoO_4 local coordination configuration. All fitting parameters are within reasonable ranges, confirming the reliability of the fitting model. Notably, Co^{2+} possesses partially occupied 3d orbitals and can retain unpaired electrons in a four-coordinated oxygen environment, providing a structural basis for the formation of localized spin-polarized electronic states [55].

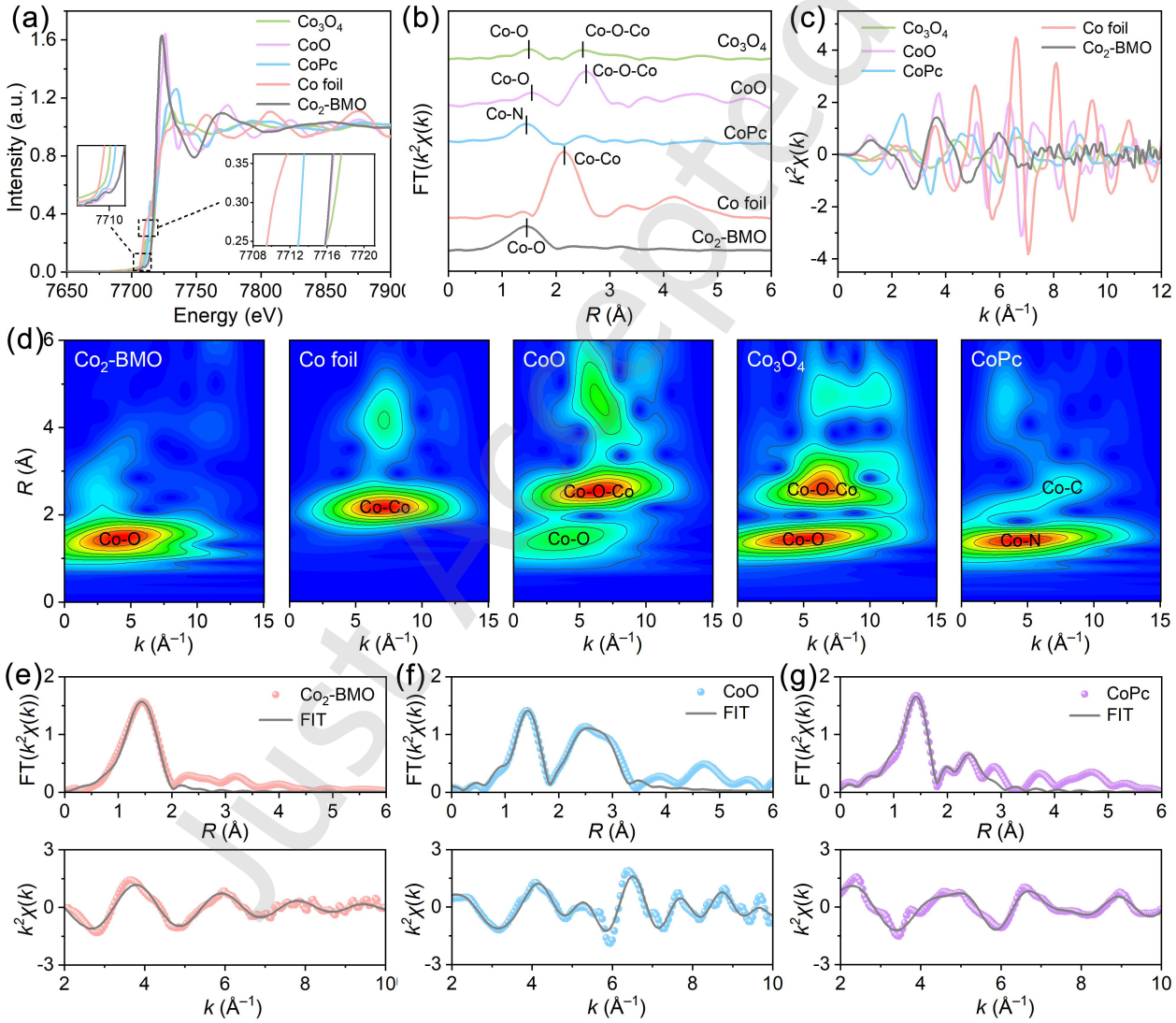


Fig. 3. Co K-edge XAFS analyses of Co_2-BMO and reference samples (Co foil, CoO, Co_3O_4 and CoPc): (a) Co K-edge XAFS spectra; (b) k^2-weighted Fourier-transformed EXAFS spectra in *R*-space; (c) k^2-weighted EXAFS oscillation curves in *k*-space; (d) wavelet transformed EXAFS images; (e–g) EXAFS fitting curves at *R*-space and *k*-space.

Just Accepted

3.2. Photocatalytic CO_2 reduction performances

The photocatalytic CO_2 reduction performance of pristine BMO and Co-doped BMO samples was evaluated under simulated solar irradiation using a 300 W Xe lamp. CO was found to be the dominant reduction product for all tested samples and only a minor amount of CH_4 was detected as a byproduct. The average yield rates of CO and CH_4 within a reaction period of 4 h over the photocatalysts are presented in Fig. 4(a) for comparison. Obviously, the Co doping dramatically accelerates CO_2 photoreduction, and the CO evolution rate follows a volcano-type trend with increasing Co dosage. The Co_2-BMO delivers the optimal photocatalytic activity with a CO production rate of 158.47 μmol g^{-1} h^{-1}, approximately 3.8 times that of pristine BMO (41.67 μmol g^{-1} h^{-1}). Such a prominent improvement in photocatalytic activity suggests that appropriate Co doping effectively modulates the electronic configuration of BMO and elevates the utilization efficiency of photogenerated charge carriers. The selectivity of CO formation includes product selectivity and electron selectivity, which can be calculated according to Eq. (1) and (2), respectively [56].

$$\text{Product selectivity (CO)}=\left(\frac{n(\text{CO})}{n(\text{CH}_4)+n(\text{CO})}\right)\times 100\% \quad (1)$$

$$\text{Electron selectivity (CO)}=\left(\frac{n(\text{CO})\times 2}{n(\text{CH}_4)\times 8+n(\text{CO})\times 2}\right)\times 100\% \quad (2)$$

Where n(CO) and n(CH_4) represent the molar yields of CO and CH_4 in a certain period, respectively. The calculated product and electron selectivities for CO formation over the photocatalysts are presented in Fig. 4(b) and (c), respectively, revealing that all samples exhibit a high selective generation of CO. In particular, the product selectivity and electron selectivity toward CO over Co_2-BMO reach 98.2% and 93.3%, respectively.

To examine the effect of Bi^0 nanocrystals formed on the photocatalyst surface on photocatalytic performance, the CO_2 photoreduction performance of the Co_2-BMO after the removal of surface Bi^0 nanocrystals by nitric acid treatment was investigated for comparison (Fig. 4(d)). It is observed that the Bi^0 elimination delivers a CO evolution rate of 115.43 μmol g^{-1} h^{-1},

Just Accepted

which is obviously lower than that of untreated Co_2-BMO. This result indicates that the in-situ formed Bi^0 nanocrystals on the photocatalyst surface are not a merely byproducts but important cocatalyst species that can enhance photocatalytic activity. On the other hand, although the removal of Bi^0 elimination results in a decline in the CO evolution rate, the rate remains much higher than that of pristine BMO, suggesting that Co doping in the BMO lattice plays a crucial role in boosting the CO_2 photoreduction performance.

To identify the carbon origin of produced CO and exclude possible interference from experimental impurities, a series of control experiments were carried out (Fig. 4(e)). Negligible CO and CH_4 signals were detected in the absence of photocatalyst, light, H_2O or CO_2 (CO_2 is replaced by Ar gas). Such outcomes indicate that the CO generation strictly relies on four indispensable prerequisites, i.e., the presence of photocatalyst, light irradiation, H_2O proton source and CO_2 reactant. Specifically, CO_2 functions as the exclusive carbon source for CO generation, while H_2O serves as the proton donor to facilitate the proton-coupled electron transfer of CO_2 activation and reduction reactions [57]. ^{13}C isotope-labeled $^{13}CO_2$ was further used as the carbon source to investigate the photoreduction of $^{13}CO_2$ over Co_2-BMO, and the reduction products were probed via mass spectrometry. The derived mass spectrum in Fig. 4(f) shows a strong signal at m/z = 29 and a weak signal at m/z = 17, which correspond to ^{13}CO and $^{13}CH_4$, respectively. The detection of these signals provides convincing evidence for the photoreduction of $^{13}CO_2$ into ^{13}CO with minor $^{13}CH_4$.

Cyclic photocatalysis tests (Fig. 4(g)) reveal that Co_2-BMO retains a high CO production rate of 152.91 μmol g^{-1} h^{-1} after five successive reaction cycles, corresponding to 96.5% activity retention relative to the initial cycle. Further analyses by XRD and SEM (Fig. S6) demonstrate that the photocatalytic cycling does not cause any detectable changes in the structure and morphology of Co_2-BMO. These results manifest that the presently developed photocatalysts exhibit satisfactory reusability and excellent stability in photocatalytic CO_2 reduction. The

Just Accepted

photocatalytic performance of Co_2-BMO and other typical bismuth-based semiconductor photocatalysts reported recently are compared in Fig. 4(h); more detailed photocatalytic test conditions and parameters are presented in Table S4. It is seen that the Co_2-BMO photocatalyst developed in this work stands out over other typical Bi-based photocatalytic systems, corroborating that the synergistic modulation strategy integrating the Co doping and in-situ generation of Bi^0 nanocrystals is particularly effective in boosting the CO_2 photoreduction activity of BMO.

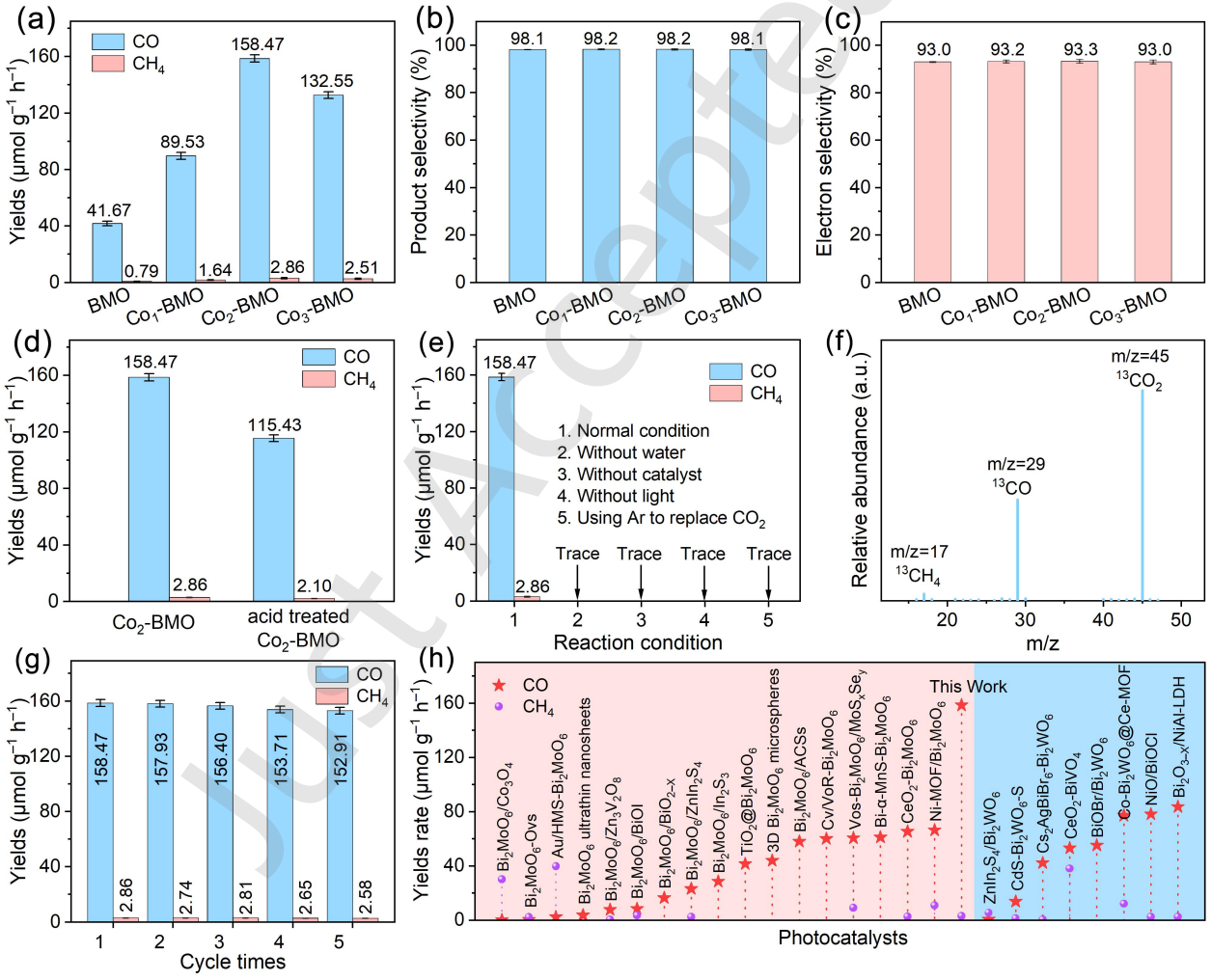


Fig. 4. (a) Average yield rates of CO and CH_4 within a reaction period of 4 h over BMO and Co_{doped}-BMO samples; (b) product selectivities and (c) electron selectivities towards CO over various photocatalysts; (d) influence of nitric acid treatment on the photocatalytic performance of Co_2-BMO; (e) control experiments for CO_2 photoreduction under different reaction conditions; (f) mass spectral analysis for isotope-labeled $^{13}CO_2$

Just Accepted

photoreduction over Co_2-BMO; (g) reusability of Co_2-BMO for CO_2 photoreduction; (h) CO_2 photoreduction performance comparison between Co_2-BMO in this work and various reported Bi-based photocatalysts.

3.3. Photocatalytic mechanism analyses

The aforementioned XAFS results demonstrate that Co species are stabilized in the BMO lattice with an atomically dispersed CoO_4 coordination structure. Owing to the relatively weak crystal field effect in the four-coordinated oxygen environment, Co^{2+} ($3d^7$) centers tend to retain unpaired 3d electrons, providing a local electronic basis for the formation of a spin-polarized electronic structure [58]. To further elucidate the influence of Co doping on the electronic structure and spin behavior of BMO, DFT calculations were performed to analyze the electronic density of states (DOS) of BMO and Co-BMO systems. The chemical composition analysis shows that the optimal Co_2-BMO has a chemical formula close to the stoichiometric composition $Bi_{1.9}Co_{0.1}MoO_6$. Therefore, a 2×1×1 supercell with one Bi atom substituted by one Co atom, i.e. $Bi_{1.875}Co_{0.125}MoO_6$ ($Bi_{15}Co_1Mo_8O_{48}$), was used to model the Co-doped BMO system for the DFT calculation (Fig. S7). The Co concentration in this computational model is close to the experimentally optimized composition and was selected as a practical approximation within the finite supercell.

As shown in Fig. 5(a) and (b), the electronic states of pristine BMO exhibit nearly symmetric distributions between spin-up and spin-down channels, indicating a typical spin-degenerate electronic structure. In contrast, after Co incorporation, the Co-BMO system exhibits an obvious asymmetric distribution between spin-up and spin-down states, particularly with the emergence of spin-splitting electronic states near the Fermi level. This result indicates that the Co 3d orbitals strongly interact with neighboring O 2p orbitals, breaking the intrinsic spin balance of BMO and inducing a spin-asymmetric electronic configuration. Further analysis of the local electronic structure around Co reveals that the unpaired 3d electrons of Co^{2+} centers generate spin polarization within the lattice environment, resulting in the redistribution of

Just Accepted

electronic states in both energy and spin orientation [58,59].

To experimentally verify the spin-polarized behavior predicted by theoretical calculations, the room-temperature magnetic properties of BMO and Co_2-BMO were investigated using a VSM under an applied magnetic field ranging from −20,000 to 20,000 Oe. As shown in Fig. 5(c), the M−H curve of BMO exhibits an approximately linear negative slope, characteristic of diamagnetic behavior, which is consistent with its spin-paired electronic configuration. In comparison, the magnetization curve of Co_2-BMO exhibits a positive response and a hysteresis loop with a detectable coercive field and remanent magnetization, indicating weak ferromagnetic behavior. This transition can be attributed to the unpaired 3d electrons introduced by Co doping, which endows the material with distinct magnetic properties. This phenomenon is consistent with the tendency of Co^{2+} ions to retain partially unpaired 3d electrons in a weak crystal-field Co–O coordination environment, further supporting the formation of a spin-polarized electronic structure [23]. These results suggest that Co incorporation not only regulates the local electronic structure of BMO but also induces spin-asymmetric electronic states, providing an electronic foundation for subsequent interfacial charge regulation and optimization of carrier dynamics during photocatalytic reactions.

To further investigate the interfacial electronic regulation mechanism between Bi^0 nanocrystals and Co-BMO, the Fermi levels and CB/VB band potentials of the photocatalysts need to be determined. The work functions of BMO (010), Co-BMO (010) and Bi^0 (001) were calculated by using DFT to be 5.37, 4.71 and 4.17 eV, respectively, as shown in Fig. 5(d−f). The corresponding structural models used for the work function calculations are shown in Fig. S8. It is noted that the Co doping in BMO results in a decrease in the work function, indicating that less energy is required for photoelectron transfer at the photocatalyst surface. According to the relationship between work function (Φ) and Fermi level (E_F), i.e. $E_F = \Phi - 4.5 - 0.059 \times pH$ (*vs.* NHE, pH = 7) [60], the Fermi levels of Co-BMO and Bi^0 are obtained to be −0.20, and −0.44 eV

Just Accepted

vs. NHE, respectively. The difference between the Fermi levels of Co-BMO and Bi^0 provides the driving force for interfacial free electron redistribution. The band-edge potentials of BMO and Co_2-BMO are estimated by measuring the Mott−Schottky plots. As shown in Fig. S9, the negative slopes of the Mott-Schottky plots suggests that the generated flat-band potentials for both samples can approximately represent their CB-edge positions [61], i.e., −0.55 V for BMO and −0.61 V for Co_2-BMO with reference to NHE at pH = 7. The slight negative shift of the conduction band induced by the Co doping provides more favorable reduction capability for CO_2 conversion. The optical properties and bandgaps of BMO and Co_2-BMO were investigated by UV−vis DRS (Fig. 5(g)). Compared with pristine BMO, the Co-doped sample exhibits enhanced visible-light absorption; particularly, a LSPR absorption band originating from Bi^0 nanocrystals is detected around 550 nm [62]. The band gaps (E_g) are obtained from the Tauc plots (Fig. S10) to be 2.90 eV for BMO and 2.83 eV for Co_2-BMO. The slightly narrowed bandgap and enhanced optical absorption contribute to an improvement in light-harvesting capability.

The above-analyzed band positions reveal that Bi^0 has a higher Fermi level than Co_2-BMO. The different Fermi level positions indicate that the in-situ growth of Bi^0 nanocrystals on the Co_2-BMO surface will result in interfacial charge redistribution, i.e., the thermally-generated electrons (free electrons) spontaneously migrate from Bi^0 to Co_2-BMO until Fermi-level equilibration is achieved. The interfacial charge redistribution generates an interfacial electric field (IEF) directed from Bi^0 toward Co_2-BMO and simultaneously induces energy band bending at the interface, as schematically depicted in Fig. 5(h). The charge redistribution at the Bi^0/Co-BMO interface is further clarified through differential charge density calculation. As shown in Fig. S11(a), the formation of the Bi^0/Co-BMO heterojunction results in the electron depletion at the Bi^0 interfacial region and electron accumulation at the Co-BMO interfacial region, indicating that free electrons spontaneously migrate from Bi^0 to Co-BMO due to their work function difference [63]. The calculated electrostatic potential (Fig. S11(b)) shows that the charge

Just Accepted

redistribution at the Bi^0/Co-BMO interface generates a potential difference of 3.67 eV between Bi^0 and Co-BMO. The formed IEF and resulting energy band bending provide a driving force for the interfacial migration of photogenerated carriers.

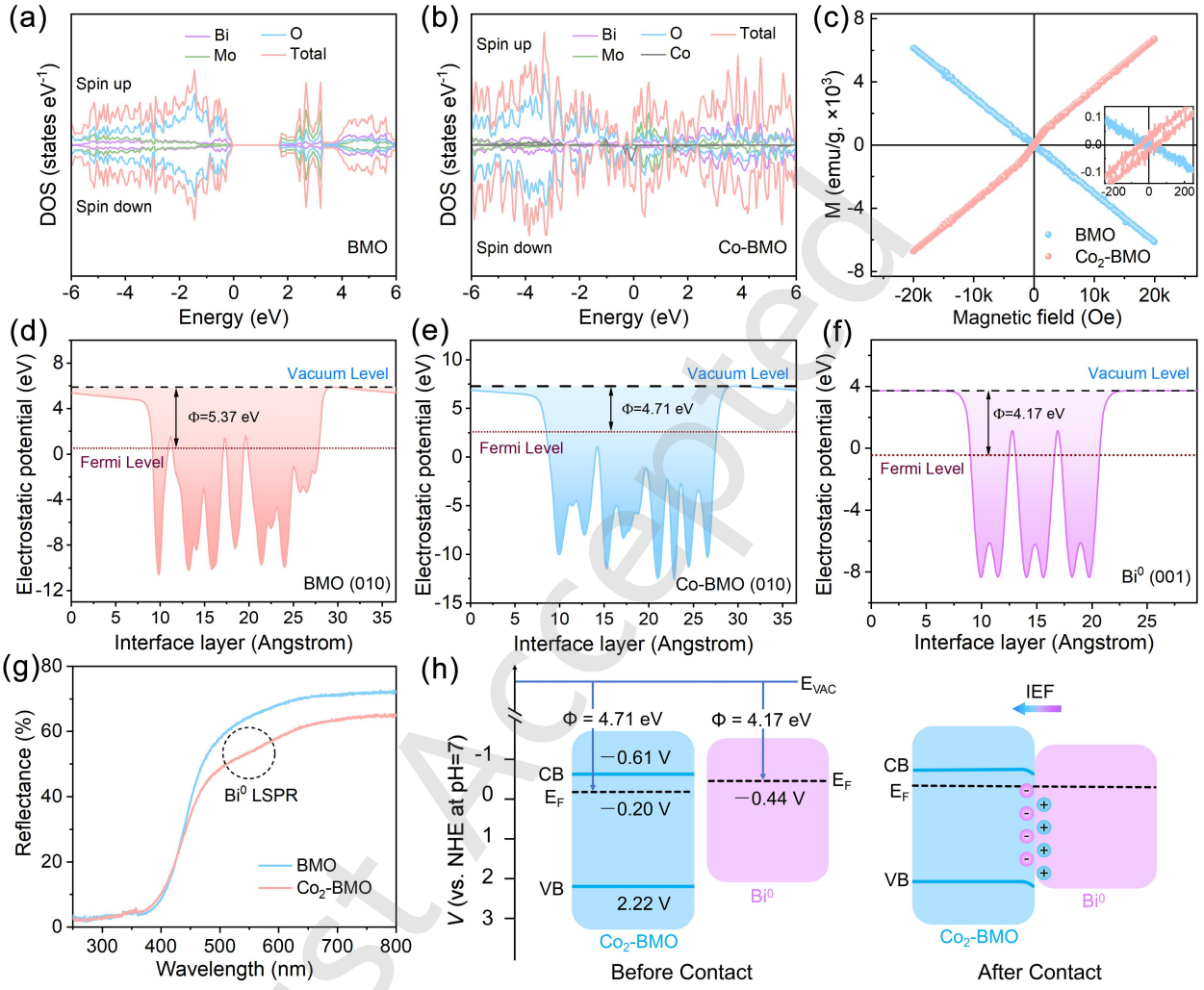


Fig. 5. Density of electronic states of (a) BMO and (b) Co-BMO; (c) VSM-measured M–H curves of BMO and Co_2-BMO at room temperature; calculated work functions of (d) BMO, (e) Co-BMO and (f) Bi; (g) UV–vis DRS profiles of BMO and Co_2-BMO; (h) schematic band alignments of BMO and Co_2-BMO before contact and the formed Bi/Co_2-BMO heterojunction.

The photocarrier separation behavior was elucidated by photoelectrochemical and PL measurements. The acquired electrochemical impedance spectroscopy (EIS) Nyquist plots (Fig. 6(a)) demonstrate that the Co_2-BMO delivers a smaller arc radius in the EIS Nyquist plot as

Just Accepted

compared with pristine BMO. When the Co_2-BMO is treated with nitric acid to eliminate the decorated Bi^0 nanocrystals, the arc radius in the EIS Nyquist plot increases but remains significantly smaller than that of pristine BMO. The EIS result manifests that the Co doping-induced spin polarization is capable of promoting the dissociation and separation of photoinduced electron-hole pairs, and the photocarrier separation efficiency can be further improved by the decoration of Bi^0 nanocrystals in combination with the Co doping-induced spin polarization. The measured transient photocurrent response plots (Fig. 6(b)) show that the photocurrent magnitude of the photocatalysts follows the order: BMO < Co_2-BMO (nitric acid-treated) < Co_2-BMO (untreated); while the probed PL intensity of the photocatalysts (Fig. 6(c)) follows the order: BMO > Co_2-BMO (nitric acid-treated) > Co_2-BMO (untreated). The photocurrent and PL analyses further verify that the Co doping-induced spin polarization efficiently promotes the photocarrier separation, which is further enhanced by simultaneous decoration of Bi^0 nanocrystals on the photocatalyst surface.

Previous studies have demonstrated that the photocatalytic reduction reactions of CO_2 necessitate the efficient adsorption of CO_2 molecules on the photocatalyst surface active sites [64,65]. For bismuth-based oxide photocatalysts, Bi sites are generally regarded as the primary sites for the CO_2 photoreduction reactions [66]. The adsorption behaviors of CO_2 on different sites of BMO (Bi site), Co-BMO (Bi site), Co-BMO (Co site) and Bi^0@Co-BMO (Bi^0 site) were elucidated by calculating the adsorption energies using the DFT method. The calculated CO_2 adsorption energies along with differential charge density distributions are presented in Fig. 6(d). For pristine BMO, the CO_2 adsorption energy at the Bi sites is obtained to be −0.92 eV; when Co is doped into the BMO lattice, the CO_2 adsorption energy at the Bi sites of Co-BMO increases to −1.96 eV. This result suggests that the electronic structure modulation by Co doping enhances the CO_2 capture and activation capability of neighboring Bi sites. Meanwhile, the Co sites exhibit a stronger CO_2 capture capability with adsorption energy of −2.36 eV, indicating that the isolated

Just Accepted

Co centers can serve as effective CO_2 photoreduction sites. For the Bi^0/Co-BMO system with Bi^0 nanocrystals decorated on the Co-BMO surface, the CO_2 adsorption energy at the Bi^0 sites reaches −2.96 eV; the high adsorption energy manifests that the Bi^0 nanocrystals are expected to be an important cocatalyst capable of providing active sites for the CO_2 photoreduction reactions. Therefore, the cobalt-doping generated Bi^0/Co-BMO system not only enhances the CO_2 adsorption on the active sites, but also provides more active sites including Bi^{3+}, Co^{2+} and Bi^0 sites for CO_2 photoreduction reactions.

The Gibbs free energies for the CO_2-to-CO conversion process on different active sites were further calculated, as shown in Fig. 6(e). The results show that the initial CO_2 adsorption process exhibits a decrease in the Gibbs free energy at all mentioned active sites, indicating that the CO_2 adsorption is thermodynamically favorable. The next proton-coupled electron transfer process from $*CO_2$ to *COOH requires overcoming a high energy barrier and is identified as the rate-determining step for the CO_2 reduction into CO [67]. The calculated energy barriers for the *COOH formation on BMO (Bi site), Co-BMO (Bi site), Co-BMO (Co site) and Bi^0@Co-BMO (Bi^0 site) are 1.266, 1.193, 1.135 and 1.004 eV, respectively. Compared with pristine BMO, the Co doping decreases the energy requirement for the *COOH formation on the Bi active sites, suggesting that the constructed CoO_4 local coordination regulates the electronic environment of neighboring Bi sites and is thereby thermodynamically conducive to the reduction of CO_2 into CO. Meanwhile, relatively lower energy barriers for the *COOH formation are also observed on the Co sites in Co-BMO and Bi^0 sites in Bi^0@Co-BMO as compared with the Bi sites in pristine BMO, indicating that the Co sites and Bi^0 sites are also beneficial to the CO_2-to-CO photoreduction reactions. Additionally, the desorption process of *CO is exothermic, suggesting the easy desorption of *CO from the photocatalyst surface to produce CO molecules.

To elucidate the CO_2 photoreduction pathway, time-resolved in-situ DRIFTS was employed to monitor the evolution of CO_2 reduction intermediates during the photocatalytic process over

Just Accepted

Co_2-BMO. As shown in Fig. 6(f), various vibrational features attributable to adsorbed intermediates are observed during photocatalysis, including those associated with *CHO (1051/1071 cm^{-1}), *CH_3O (1159 cm^{-1}), b-CO_3^{2-} (1340/1459 cm^{-1}), HCO_3^- (1419/1472/1699 cm^{-1}), m-CO_3^{2-} (1394/1522/1539 cm^{-1}), *COOH (1558/1620/1651 cm^{-1}), *CH_2O (1713 cm^{-1}) and *CO (2075 cm^{-1}), based on their characteristic vibrational frequencies and comparison with previous reports [68,69]. Under dark conditions, no obvious reduction intermediates are detected, demonstrating that light irradiation is essential for CO_2 activation and subsequent reduction. Under light irradiation, the formation of carbonate species (b-CO_3^{2-}, m-CO_3^{2-} and HCO_3^-) suggests that the reactions of CO_2 with OH^- species are involved in the CO_2 adsorption and activation processes [70]. The characteristic signals of *COOH species, a crucial intermediate for the *CO_2-to-*CO conversion, are clearly detected and their intensity remains relatively stable with increasing reaction time. This reflects the continuous generation and subsequent conversion of *COOH intermediates into *CO via proton-coupled electron transfer processes. Further, the characteristic signal of *CO at 2075 cm^{-1} appears to be stable without continuous intensity accumulation, suggesting rapid desorption of *CO from the catalyst surface thereby maintaining a low surface *CO coverage. This dynamic equilibrium prevents active-site blockage by product accumulation, thereby sustaining continuous CO formation and explaining the high CO selectivity and stability of the Co_2-BMO photocatalyst. Additionally, the signals of *CHO and *CH_3O intermediates exhibit a transient increase followed by attenuation, suggesting that some *CO species may undergo further proton-coupled electron-transfer processes toward CH_4 formation. However, these intermediates are not continuously produced, indicating that the present photocatalyst exhibits preferential selectivity toward the CO pathway while suppressing excessive hydrogenation.

Just Accepted

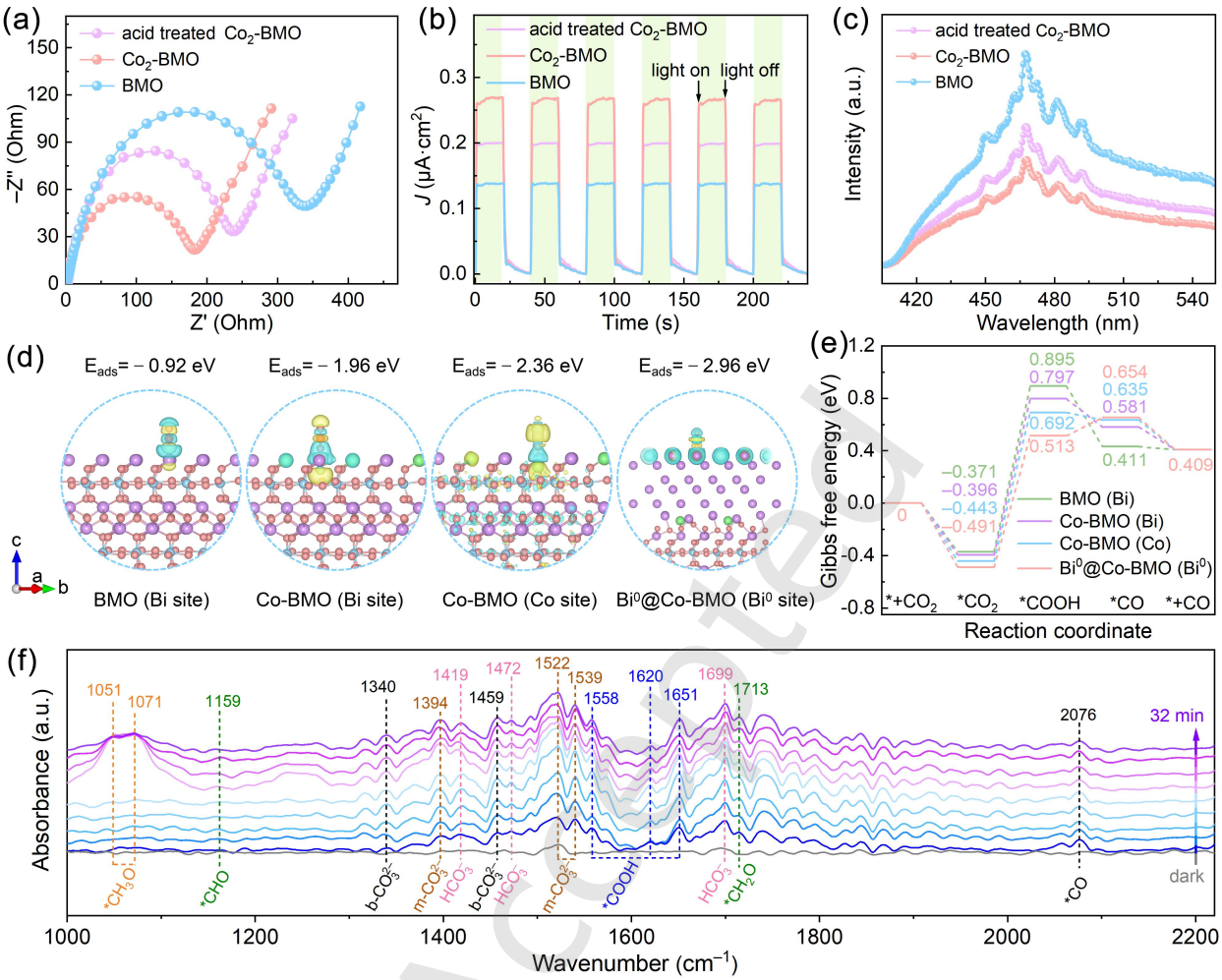


Fig. 6. (a) EIS Nyquist plots, (b) transient photocurrent responses and (c) PL spectra of pristine BMO, Co_2-BMO (untreated) and Co_2-BMO (nitric acid-treated); (d) CO_2 adsorption energies at different active sites; (e) Gibbs free energies for CO_2-to-CO reduction process at different active sites; (f) time-resolved in-situ DRIFTS spectra for CO_2 photoreduction on Co_2-BMO.

Just Accepted

The ultrafast photocarrier dynamics in the Co_2-BMO sample were further elucidated by means of fs-TA spectroscopy. The acquired fs-TA contour map (Fig. 7(a)) and corresponding spectra at different delay times (Fig. 7(b)), upon excitation with a 350 nm pump pulse, demonstrate that the Co_2-BMO exhibits pronounced negative ΔA signals in the wavelength regions of approximately 500–600 and 680–750 nm. The negative ΔA signals at around 500–600 nm may be assigned to ground-state bleaching (GSB) induced by photoexcitation, reflecting the

depletion of the ground-state population; while the negative ΔA signals at around 680–750 nm may be assigned to stimulated emission (SE), reflecting the continuous relaxation and redistribution of photoexcited carriers [71]. To reveal the distinct kinetic processes underlying the observed spectral evolution, global analysis was performed on the entire transient absorption dataset. The derived evolution-associated spectra (EAS, Fig. 7(c)), decay-associated spectra (DAS, Fig. 7(d)) and corresponding kinetic population profiles (Fig. 7(e)) reveal four characteristic dynamic components with time constants of 0.78 ps, 9.24 ps, 260.34 ps and > 7 ns. The ultrafast component of 0.78 ps can be attributed to the initial relaxation and cooling of the photoexcited carriers. The subsequent 9.24 ps component may involve the dissociation of photogenerated excitons. With increasing delay time, a slower decay component of 260.34 ps is observed, suggesting that a fraction of the photogenerated charges evolves into relatively stable charge states, i.e., spin-polarized states induced by Co doping. Notably, a long-lived component of > 7 ns is also parsed out, indicating that a fraction of the photoinduced charges can be retained on a timescale exceeding several nanoseconds due to the synergistic mechanism of Co doping-induced spin polarization and Bi^0/Co-BMO interfacial charge transfer. The kinetic trace extracted at a representative wavelength 590 nm (Fig. 7(f)) further indicates that the photoexcited carriers in the Co_2-BMO undergo multistage dynamics, particularly including a long-lived component of > 7 ns. The presence of long-lived photocarriers can extend the temporal window for photocarrier migration toward surface-active sites, thereby providing greater opportunity for their participation in subsequent CO_2 adsorption, activation and reduction reactions.

Just Accepted

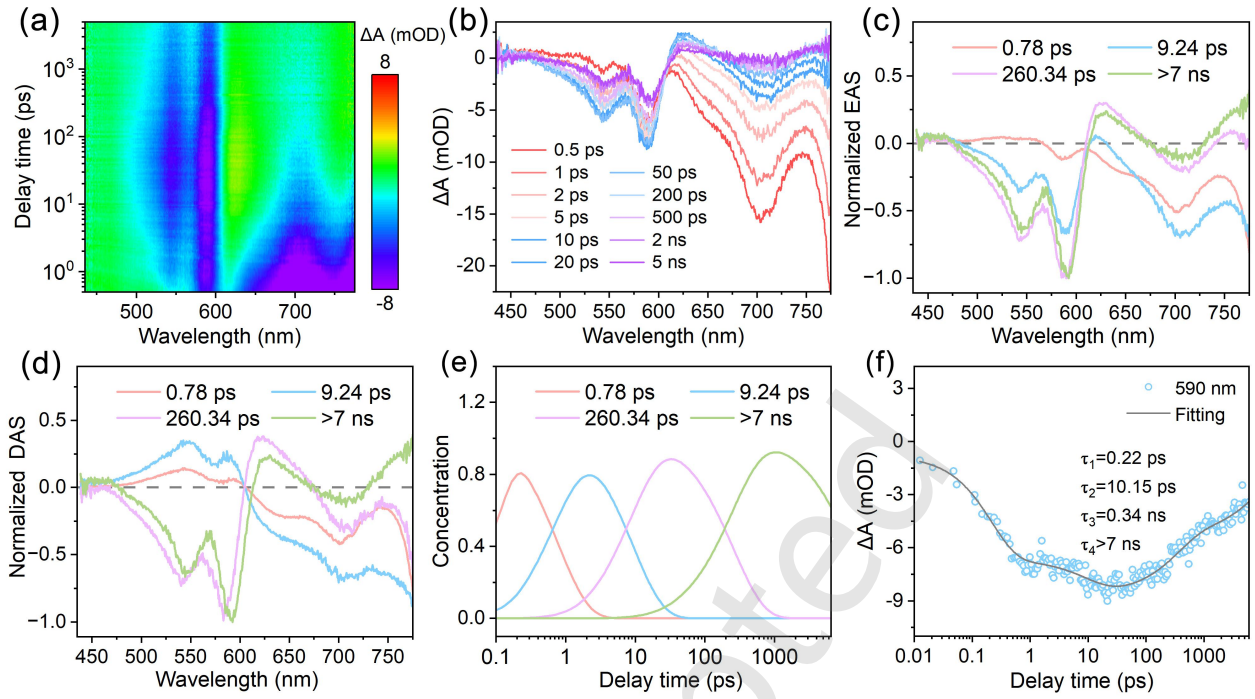


Fig. 7. (a) fs-TA contour map of Co_2-BMO; (b) transient absorption spectra at different probe delay times; (c) evolution-associated spectra, (d) decay-associated spectra and (e) population dynamics obtained by global fitting based on a four-stage dynamics model; (f) kinetic trace along with fitted curve at a representative probe wavelength 590 nm.

Just Accepted

3.4. Further discussion and summary of the enhanced photocatalytic mechanism

Based on the experimental characterizations and theoretical calculations, the mechanisms underlying the enhanced photocatalytic performance of the Co-doped BMO photocatalysts for photoreduction of CO_2 were further discussed and schematically depicted in Fig. 8. The main mechanisms are elucidated from the following aspects. (1) When Co atoms partially substitute Bi atoms in the BMO lattice, the introduction of unpaired 3d electrons from Co^{2+} disrupts the intrinsic spin-degenerate state of BMO and induces a spin-asymmetric electronic structure (i.e., spin polarization). During photoexcitation, electrons with specific spin orientations are excited from the VB to the CB, leaving holes with opposite spin orientations in the VB. Spin–orbit coupling (SOC) and hyperfine interactions (HFI) may induce partial spin flipping during electron transport, thereby modifying the relative populations of spin-up and spin-down carriers. In

non-spin-polarized BMO, the electronic states remain spin-degenerate, and photogenerated carriers exhibit approximately equal spin occupation probabilities. Therefore, even after spin changes occur, the carriers still possess a high probability of satisfying the spin-allowed recombination requirement [25], as depicted in Fig. S12. However, in the Co_{doped}-BMO system, spin polarization leads to spin-selective occupation of photogenerated electrons. When electron spin flipping occurs, the resulting spin configuration may no longer satisfy the spin conservation requirement for electron-hole recombination, potentially suppressing partial spin-allowed recombination pathways and prolonging photocarrier lifetimes for photocatalytic reactions [72], as shown in Fig. 8(a). (2) The Co doping simultaneously results in the formation of Bi^0 nanocrystals on the catalyst surface. The interfacial charge redistribution creates an interfacial electric field directed from Bi^0 toward Co_2-BMO at the Bi^0/Co-BMO interface. During the photocatalytic process, the photogenerated electrons in the CB of Co-BMO are driven to the Fermi level of Bi^0 nanocrystals by the created interfacial field. Owing to the LSPR effect of Bi^0 nanocrystals, which is identified by the UV−vis DRS analysis as well as reported in the literature [73], the accumulated photoelectrons in the CB of Bi^0 nanocrystals will be excited to the SP states under visible-light irradiation. Simultaneously, the photoelectrons in the Bi^0 SP states may flow back to the CB of Co-BMO. The cyclic transfer of the photoelectrons between Co-BMO and Bi^0 decreases the recombination of the photoelectrons with the photoholes in the VB of Co-BMO (Fig. 8(b)). Moreover, the remarkable LSPR effect of Bi^0 nanocrystals will induce local electromagnetic fields, further promoting the photocarrier generation and separation. (3) The Co incorporation regulates the electronic environment of neighboring Bi sites, thereby enhancing the CO_2 adsorption on the Bi active sites and decreasing the energy barrier for the formation of the crucial *COOH intermediate. This is beneficial to the CO_2 capture, activation and subsequent reduction. Moreover, compared with pristine BMO with single type of Bi active sites, the Co-doping generated Bi^0/Co-BMO system provides extra Co and Bi^0 active sites besides the

Just Accepted

intrinsic Bi active sites for CO_2 photoreduction reactions. The cascade synergistic mechanism involving Co doping facilitates the photocarrier generation, separation, migration and surface reactions, consequently boosting the CO_2 photoreduction performance.

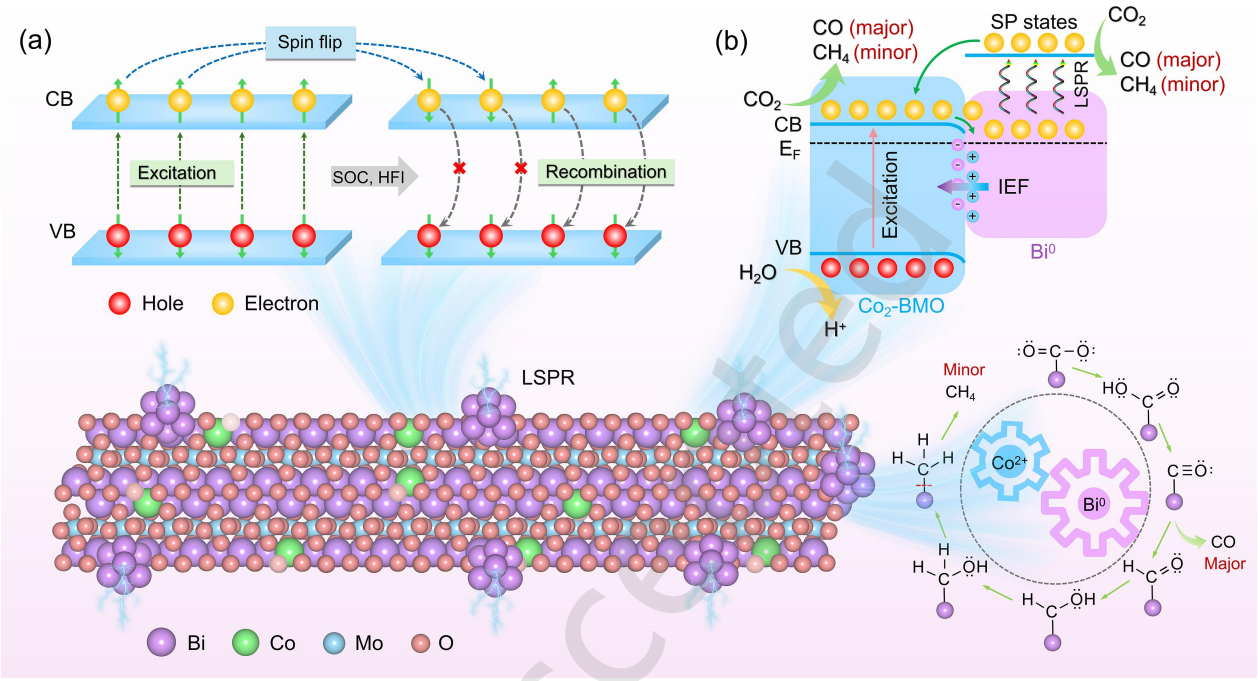


Fig. 8. Schematic diagram depicting the enhanced CO_2 photoreduction mechanism of Co-doped BMO photocatalysts: (a) structural model of Bi^0/Co-BMO; (b) spin flipping induced suppression of photocarrier recombination in spin-polarized Co-BMO; (c) photocarrier transfer and separation mechanism; (d) photoreduction pathways of CO_2 into CO (major) and CH_4 (minor).

4. Conclusion

In summary, Co-doped and surface Bi^0 nanocrystal-modified BMO photocatalysts were prepared through a facile one-step solvothermal method, achieving the synergistic integration of multiple factors to boost CO_2 photoreduction performance. Experimental characterizations and theoretical calculations demonstrate that the Co doping generates CoO_4 local coordination configuration, breaking the intrinsic spin degeneracy of BMO and generating spin-polarized electronic states. The spin polarization induced by the Co doping efficiently suppresses the recombination of photogenerated carriers. The Co doping simultaneously generates Bi^0

Just Accepted

nanocrystals on the Co-BMO surface, further facilitating the photocarrier separation by the Bi^0/Co-BMO interfacial electric field and LSPR effect of Bi^0 nanocrystals. Moreover, the Co doping not only increases the CO_2 adsorption energy on the Bi active sites, but also decreases the energy barrier for the key *COOH intermediate formation, which is beneficial to CO_2 capture, activation and reduction. In addition to the intrinsic lattice Bi active sites, the Co-doping induced Bi^0/Co-BMO system generates extra Co and Bi^0 active sites for the CO_2 photoreduction reactions. Benefiting from the synergistic effect of these factors, the Co-doped BMO photocatalysts exhibit much enhanced performance for photocatalytically converting CO_2 into CO. Particularly, the optimal Co_2-BMO photocatalyst achieves a CO yield rate of 158.47 μmol g^{-1} h^{-1}, which is 3.8 times higher than that of pristine BMO, and the CO product selectivity (or electron selectivity) reaches as high as 98.2% (or 93.3%). This work provides insights into the rational design of photocatalysts through the synergistic effects of spin polarization and interfacial charge transfer for enhanced photocatalytic CO_2 reduction.

Acknowledgements

This work was supported by the National Natural Science Foundation of China (Grant No. 52162040).

References

[1] Wagner, A.; Sahm, C. D.; Reisner, E. Towards molecular understanding of local chemical environment effects in electro- and photocatalytic CO_2 reduction. *Nat. Catal.* 2020, 3, 775–786.

[2] Zhang, F. Y.; Liu, G. R.; Sun, X. F.; Dai, Y. Y.; Ma, J. Y.; Xian, T.; Yang, H. Dual built-in electric fields in NiCo-LDH/Co_9S_8/Ag hollow nanocages synergistically boost solar-driven CO_2 photoreduction. *Sep. Purif. Technol.* 2025, 379, 134913.

[3] Wu, X.; Zhang, W. L.; Li, J.; Xiang, Q. J.; Liu, Z. Y.; Liu, B. Identification of the Active Sites on Metallic MoO_{2-x} Nano-Sea-Urchin for Atmospheric CO_2 Photoreduction Under UV, Visible, and Near-Infrared Light Illumination. *Angew. Chem. Int. Ed.* 2023, 62, e202213124.

[4] Li, M. J.; Wen, X. H.; Ke, Z. Y.; Huang, C.; Wang, S.; Lin, X.; Shen, R. C.; Luo, J. M.; Li, X. Cocatalyst

Just Accepted

Engineering in Covalent Organic Frameworks Boosts Photocatalysis. *Adv. Sustain. Syst.* 2026, 10, 28.

[5] Kreft, S.; Wei, D.; Junge, H.; Beller, M. Recent advances on TiO_2-based photocatalytic CO_2 reduction. *EnergyChem* 2020, 2, 100044.

[6] Zhang, R. Y.; Qiao, Q. Q.; Yu, B. H.; Zhang, Z. H.; Wang, J. A.; Li, S.; Liu, Y. J.; Yuan, H. D.; Luo, J. M.; Wang, Y.; et al. Formation of CeO_2/NiO composites with intergrowth superstructures for photocatalytic CO_2 reduction. *Nano Res.* 2025, 18, 94907657.

[7] Liang, C. J.; Zhu, X. N.; Zhao, Z. W.; Teng, Z. Y.; Ma, Q. F.; Gan, H. H.; Li, J. Leveraging Photothermal Effects for Efficient CO_2 Reduction: Bridging Mechanistic Understanding and Material Performance. *Adv. Funct. Mater.* 2026, 0: e78134.

[8] Jabbar, Z. H.; Graimed, B. H.; Radeef, A. Y. Recent advances in Bi_2MoO_6-based photocatalysts: structural engineering, charge transfer mechanisms, and emerging applications in CO_2 reduction and N_2 fixation. *Inorg. Chem. Commun.* 2026, 191, 117000.

[9] Di, J.; Zhao, X. X.; Lian, C.; Ji, M. X.; Xia, J. X.; Xiong, J.; Zhou, W.; Cao, X. Z.; She, Y. B.; Liu, H. L.; et al. Atomically-thin Bi_2MoO_6 nanosheets with vacancy pairs for improved photocatalytic CO_2 reduction. *Nano Energy* 2019, 61, 54–59.

[10] Fan, J. S.; Shi, L.; Ge, H. N.; Liu, J. C.; Deng, X. Z.; Li, Z. Y.; Liang, Q. Regulating the oxygen vacancy on Bi_2MoO_6/Co_3O_4 core‐shell nanocage enables highly selective CO_2 photoreduction to CH_4. *Adv. Funct. Mater.* 2025, 35, 2412078.

[11] Kumara, G.; Dutta, R. K. Sunlight mediated photo-Fenton degradation of tetracycline antibiotic and methylene blue dye in aqueous medium using $FeWO_4/Bi_2MoO_6$ nanocomposite. *Process Saf. Environ.* 2022, 159, 862–873.

[12] Mandal, A.; Kargupta, K. Cu-doped 2D-Bi_2MoO_6 nanoribbon/rGO photocatalysts for selective ethanol production by photocatalytic CO_2 reduction. *ACS Appl. Nano Mater.* 2025, 8, 3471–3486.

[13] Zhang, X. Y.; Wang, H.; An, W. J.; Guo, H. X.; Liu, L.; Cui, W. Q. Ionic liquid promotes the efficient photocatalytic reduction of CO_2 by Cu nanodots modified oxygen-vacancy Bi_2MoO_6. *Appl. Surf. Sci.* 2023, 641, 158464.

[14] Ahmadi, M.; Alavi, S. M.; Larimi, A. Pt-Cu@Bi_2MoO_6/TiO_2 photocatalyst for CO_2 reduction. *Inorg. Chem.* 2023, 62, 20372–20389.

[15] Feng, B.; Qi, B.; Wang, S.; Zhang, P.; Shen, R.; Li, Y.; Li, X. Elucidating the Charge-Separation and

Just Accepted

Oxidation Dynamics in Fluorenone-COF/CdS S-Scheme Heterojunction for Photocatalytic Benzaldehyde and Hydrogen Production. *Energy Environ. Mater.* 2025, 9, e70153.

[16] Xu, M.; Shen, R.; Yan, Y.; Mo, Y.; Wang, S.; Zhang, P.; Li, X. Concerted Proton-Electron Transfer in an S-Scheme PTA/g-C_3N_4 Heterojunction Enables Efficient H_2O_2 Photocatalysis. *Adv. Funct. Mater.* 2026, 36, e27907.

[17] Cao, Z. Y.; Wan, Q.; Wang, F. M.; Yin, S.; Tian, M.; Hao, G. Z.; Jiang, W.; Ye, J. H.; Liu, G. G. Steering C–H activation by spin-polarized single-sites for near-unity selective and efficient photocatalytic methanol coupling to ethylene glycol. *ACS Nano* 2026, 20, 8850–8861.

[18] Sun, K.; Huang, Y.; Wang, Q. Y.; Zhao, W. D.; Zheng, X. S.; Jiang, J.; Jiang, H. L. Manipulating the spin state of Co sites in metal-organic frameworks for boosting CO_2 photoreduction. *J. Am. Chem. Soc.* 2024, 146, 3241−3249.

[19] Pan, L.; Ai, M. H.; Huang, C. Y.; Yin, L.; Liu, X.; Zhang, R. R.; Wang, S. B.; Jiang, Z.; Zhang, X. W.; Zou, J. J.; et al. Manipulating spin polarization of titanium dioxide for efficient photocatalysis. *Nat. Commun.* 2020, 11, 418.

[20] Xu, Y. S.; Sun, Q.; Wang, X. Z.; Liang, J.; Yan, X. Spin effects in photocatalysis: fundamental insights and applications. *Carbon Neutral*. 2026, 5, e70163.

[21] Zhao, L. L.; Hou, H. L.; Wang, S.; Wang, L.; Yang, Y.; Bowen, C. R.; Wang, J. G.; Liao, Z. Y.; Yang, D. J.; Yan, R. F.; et al. Engineering Co single atoms in ultrathin BiOCl nanosheets for boosted CO_2 photoreduction. *Adv. Funct. Mater.* 2025, 35, 2416346.

[22] Wang, Y.; Li, S.; Hou, X.; Cui, T.; Zhuang, Z.; Zhao, Y.; Wang, H.; Wei, W.; Xu, M.; Fu, Q.; et al. Low-spin Fe^{3+} evoked by multiple defects with optimal intermediate adsorption attaining unparalleled performance in water oxidation. *Adv. Mater.* 2024, 36, 2412598.

[23] Sun, T.; Wang, K.; Du, Y. X.; Chen, J. G.; Li, X. P.; He, Z. H.; Hao, X. D.; Wang, W. T.; Wang, H.; Liu, Z. T. Synergistic spin-polarization and ohmic contact in Co^{2+} doped ultrathin BiOCl nanosheets with Bi sub-nanoclusters for boosted CO_2 photoreduction. *Appl. Catal. B: Environ. Energy* 2026, 381, 125849.

[24] Wang, Y.; Xie, Y.; Yu, S.; Yang, K.; Shao, Y.; Zou, L.; Zhao, B.; Wang, Z.; Ling, Y.; Chen, Y. Ni doping in unit cell of BiOBr to increase dipole moment and induce spin polarization for promoting CO_2 photoreduction via enhanced build-in electric field. *Appl. Catal. B: Environ.* 2023, 327, 12242.

[25] Lin, C. C.; Liu, T. R.; Lin, S. R.; Boopathi, K. M.; Chiang, C. H.; Tzeng, W. Y.; Chien, W. H. C.; Hsu, H.

Just Accepted

S.; Luo, C. W.; Tsai, H. Y.; et al. Spin-polarized photocatalytic CO_2 reduction of Mn-doped perovskite nanoplates. *J. Am. Chem. Soc.* 2022, 144, 15718–15726.

[26] Liu, J.; Wang, H.; Chang, M. J.; Sun, M.; Zhang, C. M.; Yang, L. Q.; Du, H. L.; Luo, Z. M. Facile synthesis of BiOCl with extremely superior visible light photocatalytic activity synergistically enhanced by Co doping and oxygen vacancies. *Sep. Purif. Technol.* 2022, 301, 121953.

[27] Xia, S. H.; Yin, X.; Chen, Y. H.; Zhang, L.; Yu, J. Y.; Ding, B.; Yan, J. H. Zeeman effect-boosted spin-polarized band splitting in diluted magnetic photocatalysis semiconductors for efficient CO_2 photoreduction. *ACS Nano* 2025, 19, 1519–1529.

[28] Kawata, K.; Iguchi, S.; Naniwa, S.; Nishimoto, M.; Teramura, K. Enhanced photocatalytic conversion of CO_2 by H_2O over Ag@Cr cocatalyst-modified $ZnTa_2O_6$. *ACS Catal.* 2025, 15, 4081–4088.

[29] Guo, W. N.; Zhang, Y. Y.; Tian, J. Q.; Liu, Z. Y.; Liu, B.; Li, J. Atomic-Scale Interface Engineering in Bi/Bi_2O_3 Heterojunctions for Selective CO_2 Photoreduction to Methanol. *Nat. Commun.* 2026, 17, 983.

[30] Duflot, M.; Marchal, C.; Caps, V.; Artero, V.; Christoforidis, K.; Keller, V. Optimization of NH_2-UiO-66/TiO_2/Au composites for enhanced gas-phase CO_2 photocatalytic reduction into CH_4. *Catal. Today* 2023, 413, 114018.

[31] Wang, X. X.; Zhu, H. R.; Chen, Y. Z.; Wu, X. T.; Wen, Q.; Qi, Y. P. Self-reference SPR refractive index sensing by Au nanodisk array coupled with an Au film. *J. Opt. Soc. Am. B* 2026, 43, 2116–2124.

[32] Liu, Y. Z.; Chen, Y. Z.; Xiao, J.; Yang, Y.; Wang, X. X. On-chip full-Stokes polarimetry based on a plasmonic meta-coupler system. *Opt. Commun.* 2026, 620, 133708.

[33] Sun, X. F.; Zhang, J. Q.; Luo, M. X.; Ma, J. Y.; Xian, T.; Liu, G. R.; Yang, H. Elevating photocatalytic H_2 evolution over $ZnIn_2S_4$@Au@$Cd_{0.7}Zn_{0.3}S$ multilayer nanotubes via Au-mediating H–S antibonding-orbital occupancy. *Chem. Eng. J.* 2024, 499, 156455.

[34] Zhao, D.; Xuan, Y. M.; Zhang, K.; Liu, X. L. Highly selective production of ethanol over hierarchical Bi@Bi_2MoO_6 composite via bicarbonate-assisted photocatalytic CO_2 reduction. *ChemSusChem* 2021, 14, 1–11.

[35] Li, G. J.; Chen, Z.; Wang, Y. L.; Su, H. W.; Chen, L.; Chen, J. J.; Xiao, J. R.; Wang, R. N.; Zhang, S. L.; Zhong, Q.; et al. In situ bismuth exsolution-driven controllable $Bi/Bi_4Ti_3O_{12}$ heterointerface catalysts for enhanced photocatalytic CO_2-to-HCOOH conversion. *Angew. Chem. Int. Ed.* 2026, 65, e4308936.

[36] Guo, Z. P.; Zhang, Z.; Liu, G. R.; Yang, H.; Sun, J. H. Enhanced oxidation resistance of graphene through strain-electric coupling. *Comp. Mater. Sci.* 2026, 262, 114406.

Just Accepted

[37] Weber, M. L.; Šmíd, B.; Breuer, U.; Rose, M. A.; Menzler, N. H.; Dittmann, R.; Waser, R.; Guillon, O.; Gunkel, F.; Lenser, C. Space charge governs the kinetics of metal exsolution. *Nat. Mater.* 2024, 23, 406–413.

[38] Dai, Y. Y.; Liu, G. R.; Sun, X. F.; Ma, J. Y.; Xian, T.; Yang, H. Mn doping and ZnS nanoparticles modification on Bi_2MoO_6 to achieve a highly-efficient photocatalyst for TC degradation. *Appl. Surf. Sci.* 2025, 681, 161611.

[39] Ju, H. A.; Park, E. B.; Hwang, J.; Kim, Y. H.; Jung, M. H.; Yang, M. J.; Kim, S. J.; Lee, J.; Kim, I.; Kim, Y. S.; et al. Oxygen vacancy-induced directional ordering of Li-ion pathways for enhanced ion conducting solid electrolytes. *ACS Energy Lett.* 2024, 9, 5606–5615.

[40] Khazaee, Z.; Khavar, A. H. C.; Mahjoub, A. R.; Motaee, A.; Srivastava, V.; Sillanpää, M. Template-confined growth of X-Bi_2MoO_6 (X: F, Cl, Br, I) nanoplates with open surfaces for photocatalytic oxidation, experimental and DFT insights of the halogen doping. *Sol. Energy* 2020, 196, 567–581.

[41] Wang, Y.; Chen, C. L.; Sun, X. F.; Wang, S. F.; Yi, Z.; Liu, G. R.; Li, R. S.; Yang, H. Enhanced piezo-photocatalytic activity of Bi_2MoO_6 nanosheets: theory and experimental studies. *Ceram. Int.* 2023, 49, 36545–36559.

[42] Mazur, Ł.; Domaradzki, K.; Winiarski, P.; Bik, M.; Mikuła, A.; Dąbrowa, J.; Cempura, G.; Adamczyk, A.; Kruk, A.; Brylewski, T. Advanced characterization and functional evaluation of Ni-/Fe-doped Cu–Mn spinels as Co-free coatings for SOFC/SOEC interconnects. *J. Mater. Chem. A* 2025, 13, 32741–32764.

[43] Wang, S. F.; Li, M. Y.; Gao, H. J.; Yin, Z. J.; Chen, C. L.; Yang, H.; Fang, L. M.; Angadi, V. J.; Yi, Z.; Li, D. F. Construction of $CeO_2/YMnO_3$ and $CeO_2/MgAl_2O_4/YMnO_3$ photocatalysts and adsorption of dyes and photocatalytic oxidation of antibiotics: performance prediction, degradation pathway and mechanism insight. *Appl. Surf. Sci.* 2023, 608, 154977.

[44] Liu, G. R.; Zhang, F. Y.; Yang, W. D.; Sun, X. F.; Dai, Y. Y.; Ma, J. Y.; Yi, Z. Constructing S-Scheme heterojunctions between ReS_2 and Cu-doped NiCo-LDH: A synergistic strategy for boosted photocatalytic hydrogen production. *Mater. Today Chem.* 2026, 54, 103736.

[45] Mohammadnasabomran, S.; Márquez-Álvarez, C.; Pérez-Pariente, J.; Martínez, A. Short-channel mesoporous SBA-15 silica modified by aluminum grafting as a support for CoRu Fischer–Tropsch synthesis catalysts. *Catal. Sci. Technol.* 2021, 11, 4245–4258.

[46] Liang, Y.; Xiang, F. F.; Xue, L.; Zhao, X. J.; Tang, L.; Liu, F. J.; Guo, Z. T.; Zhan, Y. H.; Liang, F. Y.; Yang, Y.; et al. Synergy engineering of d-band center and multi-phase interface charge transport in ternary

Just Accepted

Co_3O_4/Pt/Bi_2MoO_6 hierarchical heterojunction arrays for superior VOCs sensing. *Energy Environ. Mater.* 2026, 9, e70317.

[47] Waehayee, A.; Ngamwongwan, L.; Kafizas, A.; Chankhanittha, T.; Butburee, T.; Nakajima, H.; Wannapaiboon, S.; Pornsuwan, S.; Suthirakun, S.; Siritanon, T. Enhanced photocatalytic efficiency of Bi_2MoO_6 for water and p-nitroaniline reduction via iodate (I^{5+}) substitution: Implications of small polaron formation. *Chem. Eng. J.* 2025, 519, 165082.

[48] Wang, C.; Liu, G. R.; Sun, X. F.; Ma, J. Y.; Xian, T.; Yang, H. $NaBH_4$ induces strong ferromagnetism of $Bi_2Fe_4O_9$ at room temperature. *Chin. Phys. B* 2025, 34, 127503.

[49] Ren, J. L.; Ma, Q. F.; Sun, X. F.; Wang, S. F.; Liu, G. R.; Yang, H. Interface-engineering enhanced photocatalytic conversion of CO_2 into solar fuels over S-type Co-Bi_2WO_6@Ce-MOF heterostructured photocatalysts. *J. Colloid Interface Sci.* 2025, 691, 137452.

[50] Wang, Y.; Sun, X. F.; Ma, J. Y.; Yi, Z.; Wang, S. F.; Liu, G. R.; Yang, H. Coupled piezo-pyro-photocatalysis of oxygen vacancies and Bi quantum dots co-modified $BaTiO_3$ for highly efficient removal of ciprofloxacin. *Sep. Purif. Technol.* 2024, 337, 126392.

[51] Ma, T. X.; Yang, C. M.; Guo, L.; Soomro, R. A.; Wang, D. J.; Xu, B.; Fu, F. Refining electronic properties of Bi_2MoO_6 by In-doping for boosting overall nitrogen fixation via relay catalysis. *Appl. Catal. B: Environ. Energy* 2023, 330, 122643.

[52] Paidi, V. K.; Lee, B. H.; Lee, A. T.; Beigi, S. I.; Grishaeva, E.; Vasala, S.; Glatzel, P.; Ko, W.; Ahn, D.; Hyeon, T.; et al. Ferromagnetic stability optimization via oxygen-vacancy control in single-atom Co/TiO_2 nanostructures. *Proc. Natl. Acad. Sci. U. S. A.* 2024, 121, e2409397121.

[53] Li, Y. X.; Zhang, X. Y.; Li, C. X.; Zhang, T.; Zhao, Z. Y.; Shen, Z. Q.; Wang, P. F.; Zhan, S. H. Overcoming diffusion limit in Fenton-like reactions: catalysis with localized dipole for enhanced peroxymonosulfate activation and targeted pollutant removal. *Appl. Catal. B: Environ. Energy* 2026, 391, 126651.

[54] Kroll, T.; Aristov, V. Y.; Molodtsova, O. V.; Ossipyan, Y. A.; Vyalikh, D. V.; Büchner, B.; Knupfer, M. Spin and orbital ground state of Co in cobalt phthalocyanine. *J. Phys. Chem. A* 2009, 113, 8917–8922.

[55] Figgis, B. N.; Hitchman, M. A. *Ligand field theory and its applications.* Wiley-VCH: Weinheim, Germany, 2000.

[56] Lai, K. Z.; Sun, Y. X.; Li, N.; Gao, Y. Q.; Li, H.; Ge, L.; Ma, T. Y. Photocatalytic CO_2-to-CH_4 conversion

Just Accepted

with ultrahigh selectivity of 95.93% on S-vacancy modulated spatial In_2S_3/In_2O_3 heterojunction. *Adv. Funct. Mater.* 2024, 34, 2409031.

[57] Li, G. C.; Shui, Z. Y.; Duan, X. X.; Yang, H. L.; Zhao, Z. Y.; Zhao, T.; Zhang, Z. S.; Jiang, G. X.; Ren, H. N.; Cheng, J.; et al. Unveiling the balance between catalytic activity and water resistance over Co_3O_4 catalysts for propane oxidation: the role of crystal facet and oxygen vacancy. *ACS Catal.* 2023, 13, 237–247.

[58] Li, W.; Zhang, Y.; Ran, W.; Wang, Y.; Tian, F.; Zhang, F.; Xu, M.; Zhang, D.; Li, N.; Yan, T. Spin polarization regulates photocatalytic CO_2 into hydrocarbons by Co doped BiOCl. *Appl. Catal. B: Environ.* 2024, 351, 123978.

[59] Xiong, R. Z.; Liu, F. D.; Xiao, X.; Xiao, Y. H.; Cheng, B. C.; Lei, S. J. Dual electronic-spin engineering in cobalt-doped CdS: Photocatalytic pathway switching from competing H_2 evolution to selective CO_2 reduction. *Chem. Eng. J.* 2025, 520, 166224.

[60] Mu, X.; Sun, X. F.; Yi, Z.; Wang, S. F.; Kakavandi, B.; Liu, G. R.; Yang, H. Boosting photocatalytic H_2O_2 synthesis over HKUST-1 MOFs-derived hollow HKUST-1@CuFePBA@CuS heterojunctions. *Energy Environ. Mater.* 2026, 9, e70247.

[61] Ma, C. X.; Chen, H. J.; Wang, W.; Sun, X. F.; Dai, Y. Y.; Zhang, F. Y.; Yi, Z.; Feng, W. J.; Liu, G. R. Boosting Photocatalytic H_2O_2 Production in Mn Doped Cu_2O Cubes via Oxygen Vacancies, Intermediate Energy Levels, and Dual Pathways Activated by Multivalent Manganese. *Process Saf. Environ.* 2026, 220, 109625.

[62] Khavar, A. H. C.; Mahjoub, A. R.; Najafi, S. Enhanced photocatalytic degradation of tetracycline by improving electron flux at the Schottky junction between Bi nanoparticles and MoS_2-anchored RGO. *J. Photochem. Photobiol., A* 2023, 447, 115270.

[63] Guo, S. T., Chen, H. J.; Wang, W.; Sun, X. F.; Zhang, J. Q.; Yi, Z.; Feng, W. J.; Liu, G. R. Synergistic effect of built-in electric field and mixed-valence $Mn^{2+}/Mn^{3+}/Mn^{4+}$ species in MnS/BiOCl heterostructure promotes photocatalytic H_2 production. *J. Environ. Chem. Eng.* 2026, 14, 124848.

[64] Kovacic, Z.; Likozar, B.; Hus, M. Photocatalytic CO_2 reduction: a review of Ab initio mechanism, kinetics, and multiscale modeling simulations. *ACS Catal.* 2020, 10, 14984–15007.

[65] Nie, Y.; Li, Y. F.; An, C.; Tan, X.; Hu, Z. F.; Ye, J. H.; Yu, T. Promoted selectivity of photocatalytic CO_2 reduction to C_2H_4 via hybrid Cu_xCoS_y possessing dual unsaturated sites. *Appl. Catal. B: Environ. Energy* 2024, 345, 123704.

Just Accepted

[66] Thang, N. Q.; Sabbah, A.; Putikam, R.; Huang, C. Y.; Lin, T. Y.; Hussien, M. K.; Wu, H. L.; Lin, M. C.; Lee, C. H.; Chen, K. H.; et al. Regulating COOH intermediate via rationally constructed surface-active sites of Bi_2WO_6 for solar-driven CO_2-to-CO production. *Adv. Funct. Mater.* 2025, 35, 2423751.

[67] Peng, T.; Wang, Y. Q.; Dong, C. L.; Nga, T. T. T.; Wu, B. L.; Wang, Y. D.; Guan, Q. Q.; Zhang, W. J.; Shen, S. H. BiOCl atomic layers with electrons enriched active sites exposed for efficient photocatalytic CO_2 overall splitting. *Nano-Micro Lett.* 2025, 17, 223.

[68] Huang, F. X.; Wang, F.; Liu, Y.; Guo, L. J. Cu-ZnS modulated multi-carbon coupling enables high selectivity photoreduction CO_2 to CH_3CH_2COOH. *Adv. Mater.* 2025, 37, 2416708.

[69] Sun, X. F.; Xian, T.; Sun, C. Y.; Zhang, J. Q.; Liu, G. R.; Yang, H. Enhancing CO_2 photoreduction on Au@CdZnS@MnO_2 hollow nanospheres via electron configuration modulation. *J. Mater. Sci. Technol.* 2025, 228, 256–268.

[70] Tian, J. Q.; Zhang, Y. Y.; Shi, Z. H.; Liu, Z. Y.; Zhao, Z. W.; Li, J.; Li, N.; Huang, H. W. Enabling interfacial lattice matching by selective epitaxial growth of CuS crystals on Bi_2WO_6 nanosheets for efficient CO photoreduction into solar fuels. *Angew. Chem. Int. Ed.* 2025, 64, e202418496.

[71] Kim, J. W. Practical method for achieving single-photon femtosecond time-resolved spectroscopy: transient stimulated emission. *J. Phys. Chem. Lett.* 2024, 15, 5407–5412.

[72] Li, M. Y.; Wu, S. Q.; Liu, D. N.; Ye, Z. C.; Wang, L. J.; Kan, M.; Ye, Z. W.; Khan, M.; Zhang, J. L. Engineering spatially adjacent redox sites with synergistic spin polarization effect to boost photocatalytic CO_2 methanation. *J. Am. Chem. Soc.* 2024, 146, 15538–15548.

[73] Chang, X. F.; Xie, L.; Sha, W. E. I.; Lu, K.; Qi, Q.; Dong, C. Y.; Yan, X. X.; Gondal, M. A.; Rashid, S. G.; Dai, Q. I.; et al. Probing the light harvesting and charge rectification of bismuth nanoparticles behind the promoted photoreactivity onto Bi/BiOCl catalyst by (in-situ) electron microscopy. *Appl. Catal. B: Environ.* 2017, 201, 495–502.

Just Accepted

Electronic Supplementary Material

Cobalt doping-induced spin polarization and *in-situ* Bi^0 decoration of Bi_2MoO_6 synergistically boosting photocatalytic CO_2-to-CO conversion

Yanyan Dai[1,2], Qianfei Ma[3], Xiaofeng Sun[4], Zainab Mehfooz[5], Zao Yi[6], Jinyuan Ma[1], Huaijing Chen[2], Guorong Liu[2], Zhansheng Lu[3], Hua Yang[1,2,*]

[1]State Key Laboratory of Advanced Processing and Recycling of Non-ferrous Metals, Lanzhou University of Technology, Lanzhou 730050, China

[2]School of Science, Lanzhou University of Technology, Lanzhou 730050, China

[3]College of Mathematics and Physics, Bejing University of Chemical Technology, Beijing 100029, China

[4]School of Electronic Information Engineering, Lanzhou institute of technology, Lanzhou 730050, China

[5]Institute of Physics, The Islamia University of Bahawalpur, Punjab, Pakistan

[6]School of Chemistry and Chemical Engineering, Jishou University, Jishou 416000, China

*Address correspondence to hyang@lut.edu.cn

Supporting information to https://doi.org/10.26599/NR.2026.94909275

Just Accepted

- **Raw materials**

The main raw materials and reagents used in the present study include bismuth nitrate pentahydrate ($Bi(NO_3)_3·5H_2O$, analytical grade > 99.0%), sodium molybdate dihydrate ($Na_2MoO_4·2H_2O$, analytical grade > 99.0%), cobalt nitrate hexahydrate ($Co(NO_3)_2·6H_2O$, analytical grade > 99.0%), ethylene glycol ($(CH_2OH)_2$, EG, analytical grade > 98.0%), ethanol

(CH_3CH_2OH, analytical grade > 98.0%), nitric acid (HNO_3, 70.0% ≥ analytical grade ≥ 68.0%). All the raw materials and reagents were purchased from Sinopharm Group Chemical Reagent Co., Ltd for direct use in the experiments.

- **Characterization methodologies**

The crystal structures of the prepared samples were characterized by X-ray powder diffraction (XRD) using a Bruker D8 Advance diffractometer with Cu Kα radiation (λ = 0.15406 nm) at a scanning rate of 4 °/min. The morphologies of the samples were characterized by scanning electron microscopy (SEM) on a JSM-6701F field-emission scanning electron microscope (JEOL Ltd.). Transmission electron microscopy (TEM) coupled with energy-dispersive X-ray spectroscopy (EDS) was employed to investigate the microstructure and elemental distribution of the samples on a JEM-1200EX field-emission transmission electron microscope (JEOL Ltd.). The surface chemical states and elemental compositions were analyzed by X-ray photoelectron spectroscopy (XPS) using an AXIS Supra spectrometer. Fourier transform infrared (FT-IR) spectroscopy analysis was carried out on a Spectrum Two FT-IR spectrophotometer (PerkinElmer) in the range of 500–4000 cm^{-1} using KBr powder. The local coordination environment of Co species was investigated by synchrotron X-ray absorption spectroscopy (XAS) on the wiggler beamline BL14W1 of the Shanghai Synchrotron Radiation Facility (SSRF, China). The XAS spectra were collected in transmission mode, and the acquired data were processed using standard X-ray absorption data analysis procedures. Ultraviolet-visible diffuse reflectance spectroscopy (UV–vis DRS) measurement was done on a TU-1901 double beam spectrophotometer (Beijing Purkinje General Instrument Co. Ltd.). Photoluminescence (PL) spectra were recorded on an RF-6000 fluorescence spectrophotometer with an excitation wavelength of approximately 300 nm. The magnetic properties of the samples were measured using a vibrating sample magnetometer (VSM, LakeShore, USA, model 7404/8604). A femto-TA100 spectrometer (Time-Tech Spectra) was used for the femtosecond transient

Just Accepted

absorption (fs-TA) spectroscopy measurements, powered by a regenerative amplified Ti laser system (Coherent) operating at 800 nm, 70 fs, 6 mJ/pulse, and a 1 kHz repetition rate.

- **Electrochemical measurements**

The transient photocurrents and electrochemical impedance spectroscopy (EIS) spectra of the samples were measured on a CHI660E electrochemical workstation using a three-electrode cell configuration. A platinum foil electrode and a standard calomel electrode (SCE) were used as the counter electrode and reference electrode, respectively. To prepare the working electrode, 15 mg of the photocatalyst, 0.75 mg of poly-vinylidene fluoride (PVDF) and 0.75 mg of carbon black were uniformly mixed using 1-methyl-2-pyrrolidione (NMP) as the solvent. The formed slurry mixture was uniformly coated onto a fluorine-doped tin oxide (FTO) glass substrate with an effective area 1 cm × 1 cm. 0.1 M Na_2SO_4 aqueous solution was used as the electrolyte. A 300W PLS-SXE300BF xenon lamp was employed as the light source to generate simulated sunlight. The photocurrent response was measured at a bias potential of 0.2 V. EIS measurements were conducted by applying a sinusoidal voltage pulse with amplitude of 5 mV over a frequency range of 10^{-2} to 10^5 Hz.

- **Photocatalytic CO_2 reduction testing**

The photocatalytic CO_2 reduction over the photocatalysts was tested using a Labsolar-6A fully automatic all-glass online trace gas analysis system (PerfectLight Technology Co., Ltd., China). The entire reaction setup consists of a fully enclosed quartz reactor, a vacuum system, and a gas chromatograph (FL GC9790II), operating in a gas–solid reaction mode. The detailed procedure was as follows: 20 mg of the photocatalyst was uniformly dispersed in 2 mL of deionized water and drop-cast on a glass fiber filter paper. The quartz membrane loaded with the photocatalyst was then placed at the bottom of the reactor and vacuum-dried for 1 h. Subsequently, 5 mL of degassed deionized water was injected into the reaction chamber. The system was evacuated and then filled with high-purity CO_2 gas (99.999%). This

Just Accepted

evacuation–refilling process was repeated three times to ensure complete removal of air from the reactor and achieve adsorption–desorption equilibrium. After that, the photoreduction of CO_2 was initiated under irradiation from a 300 W xenon lamp (Microsolar300, Beijing PerfectLight Technology Co., Ltd.). The light source was positioned directly above the reactor, with a distance of 5 cm between the lamp and the photocatalyst film. The gaseous products from CO_2 photoreduction were analyzed using an Agilent GC-7890B gas chromatograph equipped with a flame ionization detector (FID), a thermal conductivity detector (TCD) and a TDX-01 carbon molecular sieve column. The cycling photoreduction experiment was conducted as follows: after each run of the photoreduction experiment was completed, the gas in the reaction chamber was evacuated, followed by the injection of high-purity CO_2. After repeating this process three times, 5 mL of deionized water was injected into the chamber to initiate the next photoreduction experiment.

- **In-situ DRIFTS analyses for CO_2 photoreduction**

In-situ diffuse reflectance infrared Fourier transform spectroscopy (DRIFTS) was performed using a Nicolet iS50 FT-IR spectrometer (Thermo Fisher, USA), equipped with a custom-designed reaction cell and a liquid nitrogen-cooled HgCdTe (MCT) detector. A thin layer of the sample film was pre-deposited on the substrate located at the center of the cell. Each sample was then purged with argon gas (50 mL/min) for 1 h at 120 °C to remove all gases from the cell and those adsorbed onto the samples. After cooling the reaction cell to 30 °C, a mixture of CO_2 (5 mL/min), Ar (25 mL/min), and trace amounts of H_2O vapor was introduced into the reactor for approximately 30 min to achieve sorption equilibrium prior to irradiation. The IR signals were collected in situ via the MCT detector throughout the reaction process. **(1) Sample pre-treatment**: In a dark environment, the sample was placed in the in situ reaction cell. Each sample was purged with Ar gas (50 mL/min) at 120 °C for 1 h and then cooled to room temperature. Background and reference IR spectra were collected. **(2) Gas introduction**: Still in

Just Accepted

the dark, after the reactor cooled to 30 °C, a mixture of CO_2 (5 mL/min) and trace amounts of H_2O vapor was introduced into the reactor for approximately 30 min. IR spectra were recorded every 4 min. **(3) Illumination**: The reactor was sealed and illuminated using a 300 W xenon lamp. The sample was irradiated for 60 min, and data were collected every 4 min.

- **DFT calculation**

First-principles density functional theory (DFT) calculations were performed using the Vienna Ab initio Simulation Package (VASP)[1,2]. The projector augmented-wave (PAW) method was employed to describe the interaction between ions and electrons. The exchange–correlation interactions were initially treated using the Perdew–Burke–Ernzerhof (PBE) functional within the generalized gradient approximation (GGA). To accurately describe the electronic structures of pristine and Co-doped BMO systems, spin-polarized calculations were considered throughout the calculations. The HSE06 hybrid functional was further employed for electronic structure calculations, density of states (DOS) analysis. The plane-wave cutoff energy was set to 500 eV. The convergence criteria for electronic self-consistency and structural relaxation were set to 10^{-5} eV and 0.03 eV/Å, respectively. **(1) DOS calculations.** A 2×1×1 supercell with one Bi atom substituted by one Co atom, i.e. $Bi_{1.875}Co_{0.125}MoO_6$ ($Bi_{15}Co_1Mo_8O_{48}$), was used to model the Co_{doped}-BMO system for the DFT calculation. The electronic structures and density of states (DOS) of pristine BMO and Co-BMO were calculated using their corresponding bulk crystal structures. **(2) Work function calculations.** The BMO (010), Co-BMO (010), and Bi^0 (001) surfaces were constructed based on their respective CIF files. A vacuum layer of 10 Å was introduced on both sides of each slab along the surface normal to eliminate spurious interactions between periodically repeated slabs. The work functions were calculated as the difference

Just Accepted

between the vacuum level and the Fermi level. **(3) Heterostructure construction and interfacial charge analysis.** To investigate the interfacial electronic interactions, The contact model between Co-BMO (010) and Bi^0 (001) was constructed using the Vaspkit package. The interfacial charge redistribution and electrostatic potential were analyzed using the differential charge density, planar-averaged differential charge density and electrostatic potential, respectively, to elucidate the interfacial electronic coupling and charge-transfer behavior in the Bi^0/Co-BMO heterojunction. **(4) Adsorption energy calculations.** The adsorption energy is defined as $E_{ads} = E_{total}(\text{catalyst/CO}_2) - E_{total}(\text{catalyst}) - E_{total}(\text{CO}_2)$, where $E_{total}(\text{catalyst/CO}_2)$ is the total energy of the optimized configuration of the catalyst (001) substrate with the CO_2; $E_{total}(\text{catalyst})$ and $E_{total}(\text{CO}_2)$ are total energies of individual catalyst substrate and CO_2 molecule, respectively. **(5) Gibbs free energy calculations.** The Gibbs free energy of adsorbates or gas-phase molecules was calculated using the following formula: $\Delta G=\Delta E+\Delta E_{ZPE}+\int_0^{298.15K} C_v \, dT-T\Delta S$, where ΔE is the change of total energies, ΔE_{ZPE} is the change of zero-point energy, T is the temperature in kelvin (298.15 K is set here), C_v is heat capacity and ΔS is the change in entropy. The harmonic approximation was used for adsorbates. The ideal gas approximation was used after DFT geometry optimization. The harmonic approximation was used for adsorbates.

Just Accepted

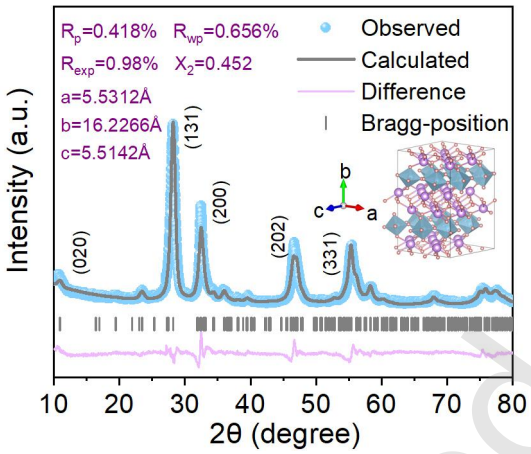


Fig. S1. Rietveld refinement of the XRD pattern of BMO.

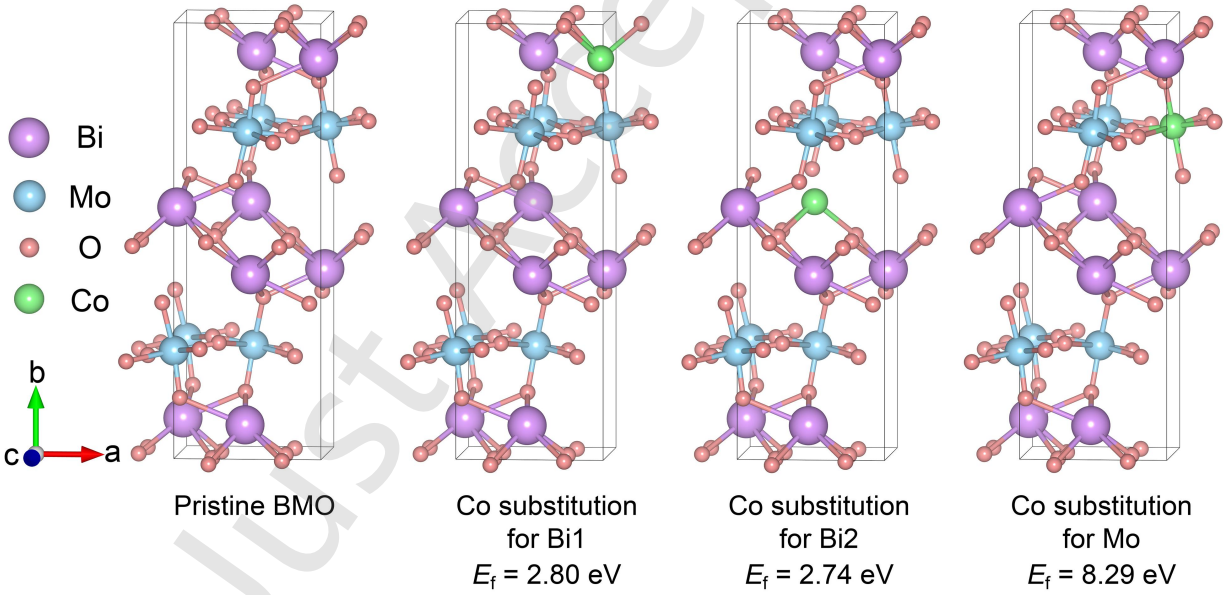


Fig. S2. Structure models of Co-BMO with Co substitution for Bi1, Bi2 or Mo along with the DFT-calculated formation energies.

Just Accepted

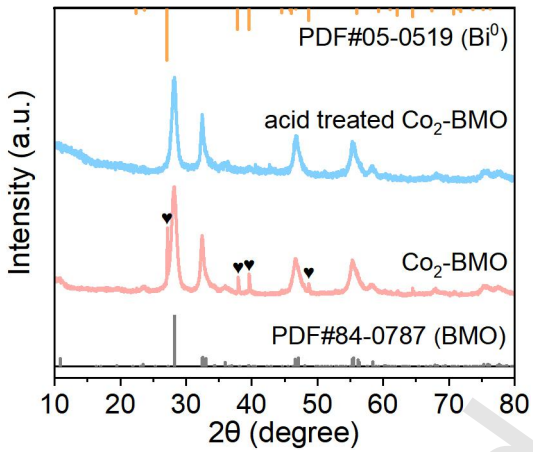


Fig. S3. XRD patterns of Co_2-BMO before and after treatment with 0.05 M dilute nitric acid.

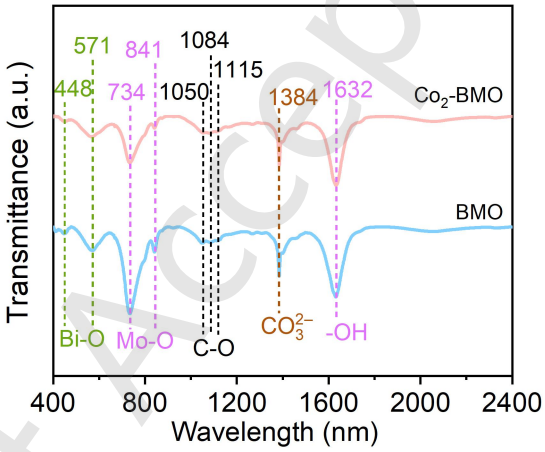


Fig. S4. FT-IR spectra of BMO and Co_2-BMO.

Just Accepted

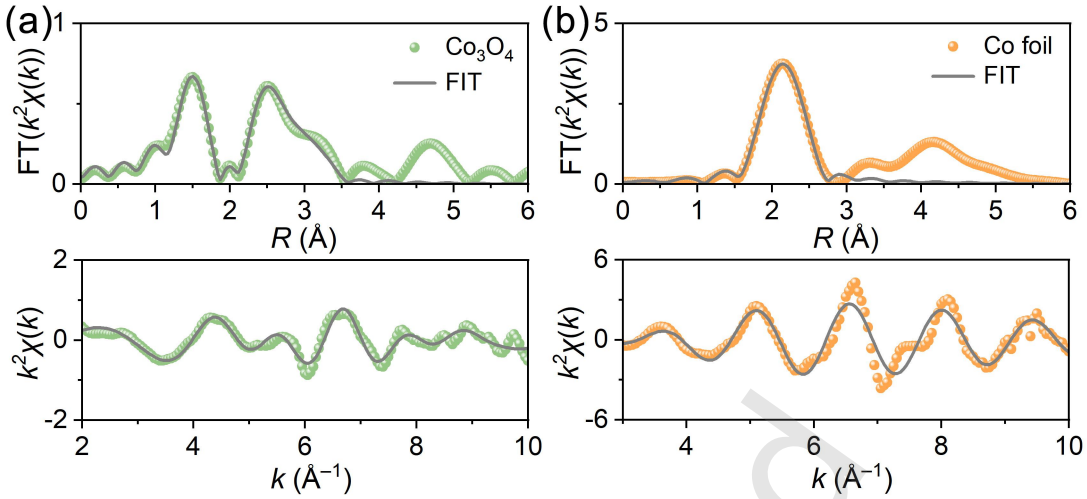


Fig. S5. EXAFS fitting curves of (a) Co_3O_4 and (b) Co foil at *R*-space and *k*-space.

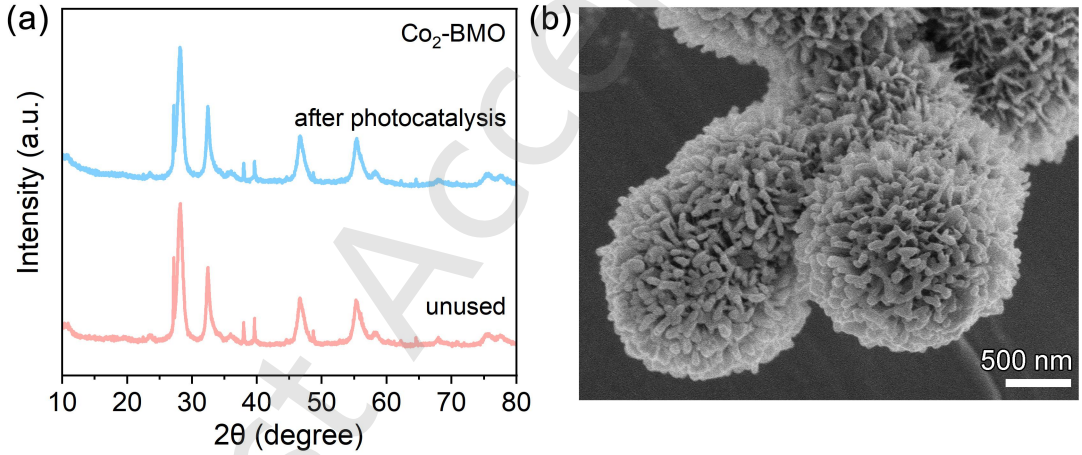


Fig. S6. (a) XRD patterns of fresh and photocatalytically used Co_2-BMO for five times; (b) SEM image of the used Co_2-BMO.

Just Accepted

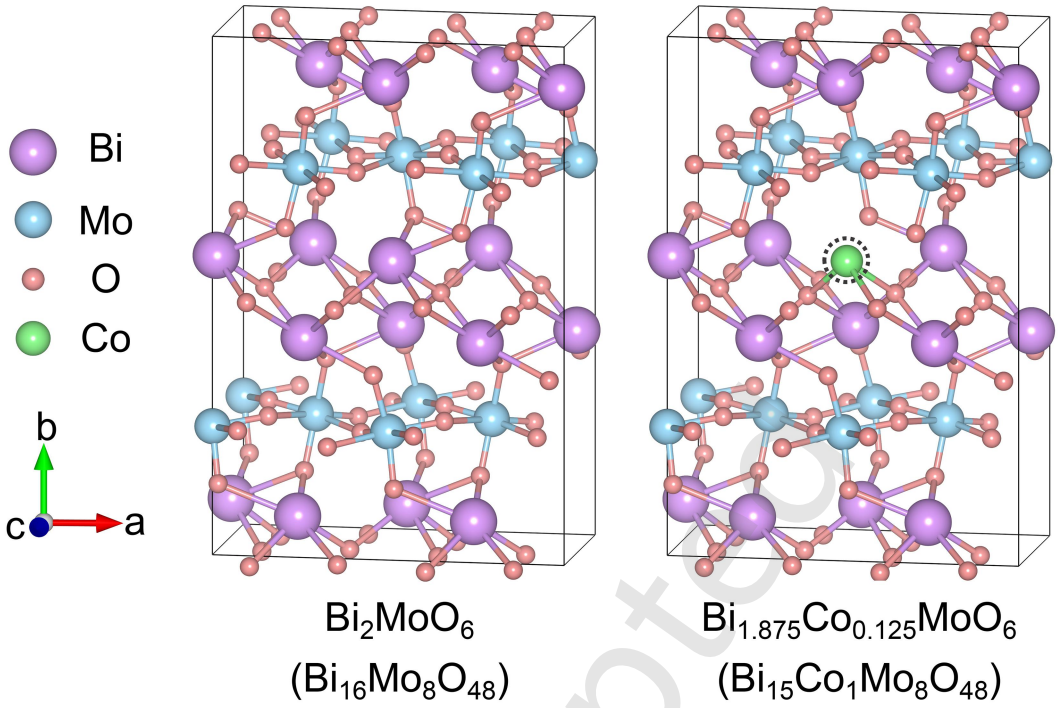


Fig. S7. Structural model of 2×1×1 BMO supercell with one Bi atom substituted by one Co atom.

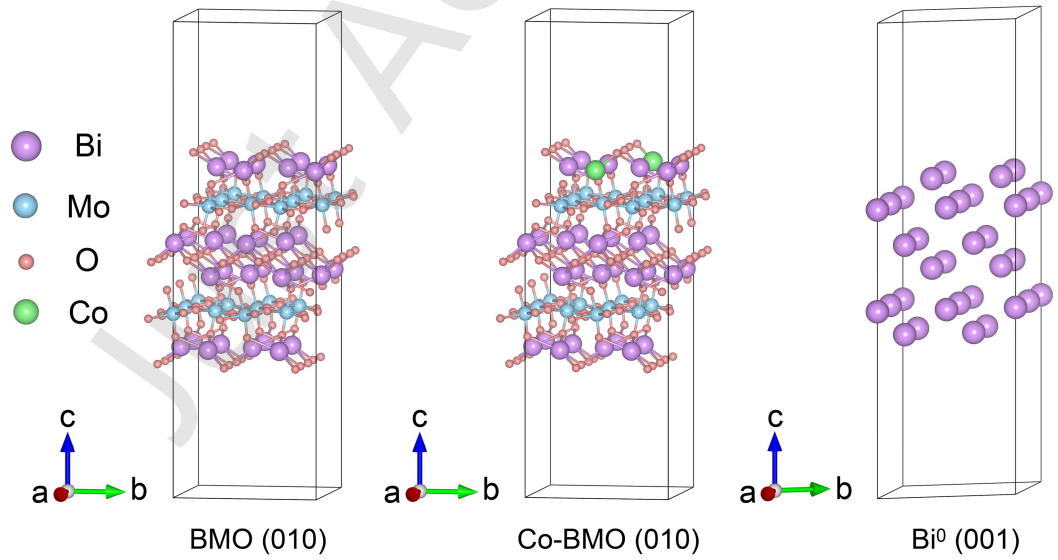


Fig. S8. Structural models of (a) BMO (010), (b) Co-BMO (010), and (c) Bi^0 (001) surfaces used for work function calculations.

Just Accepted

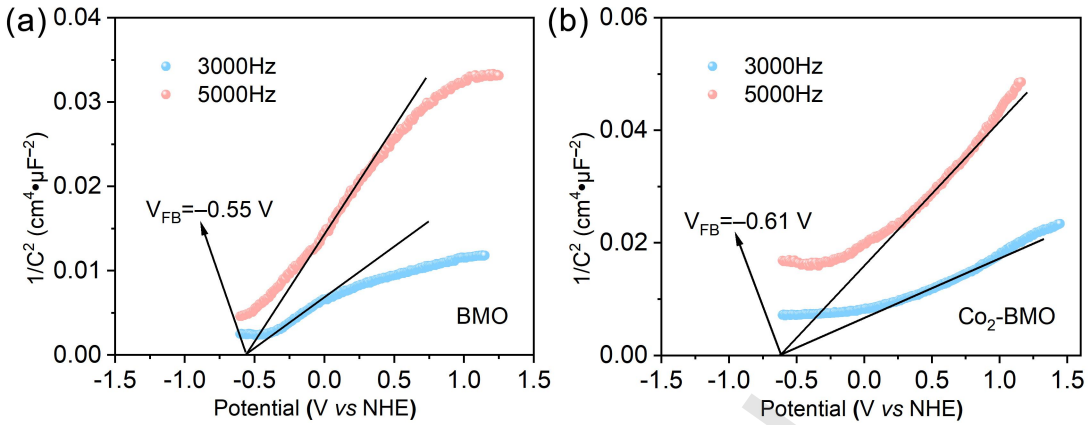


Fig. S9. Mott–Schottky plots of (a) BMO and (b) Co_2-BMO.

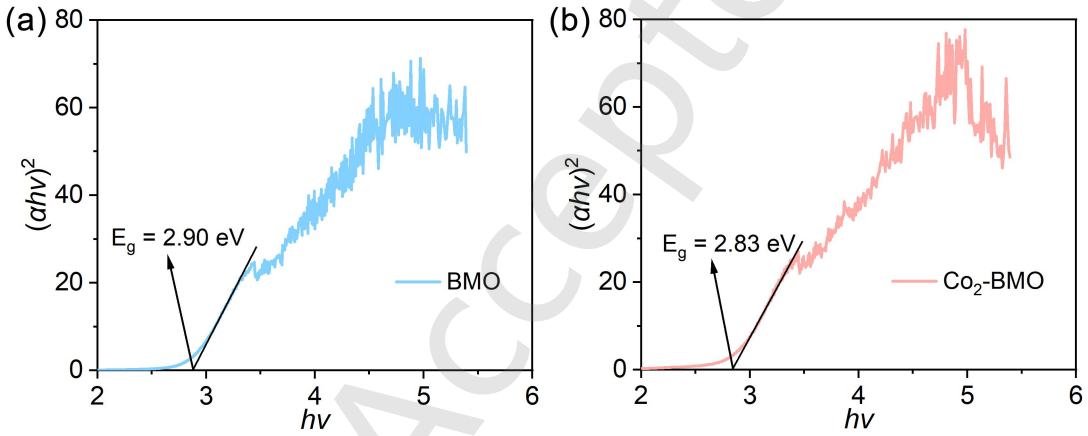


Fig. S10. Tauc plots of (a) BMO and (b) Co_2-BMO.

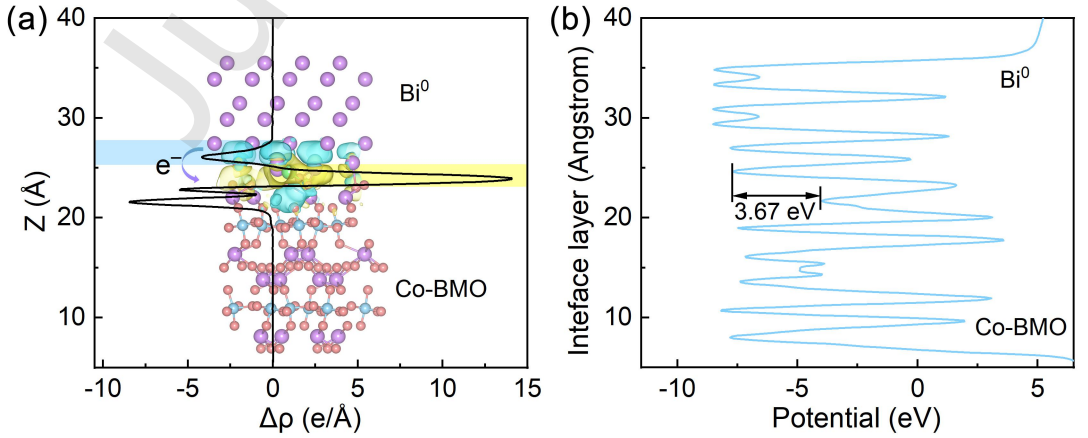


Fig. S11. (a) differential charge density image along with planar-averaged differential charge density and (b) electrostatic potential of Bi^0/Co-BMO heterojunction.

Just Accepted

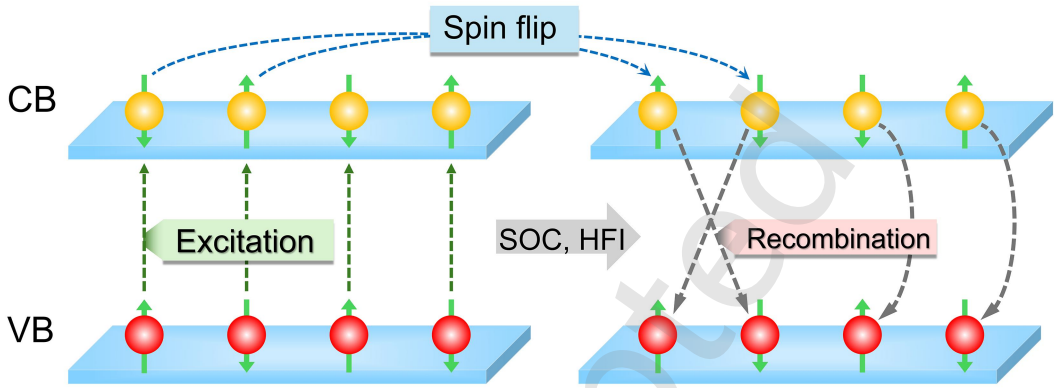


Fig. S12. Photocarrier recombination mechanism upon spin flipping in non-spin-polarized BMO.

Just Accepted

Table S1. Calculated total binding energies (eV) of various structures and elements.

Category	Structure 1 (pristine BMO)	Structure 2 (Co → Bi1)	Structure 3 (Co → Bi2)	Structure 4 (Co → Mo)	Bi	Mo	Co
Total binding energy	-252.83	-253.57	-253.63	-241.28	-3.30	-10.10	-6.84

Table S2. Content of elements (wt%) in the photocatalysts obtained by ICP-MS measurement.

Samples	Bi	Mo	Co
Co_1-BMO	70.51	16.16	0.21
Co_2-BMO	68.91	16.06	1.01
Co_3-BMO	69.57	16.08	1.82

Table S3. EXAFS fitting parameters at the Co K-edge for various samples.

Samples	shell	^aCN	^bR (Å)	$^c\sigma^2$ (Å^2)	$^d\Delta E_0$ (eV)	R-factor
Co-foil	Co-Co	12*	2.48±0.01	0.0062	6.3±0.5	0.0018
CoPc	Co-N	4*	1.97±0.02	0.0079	7.0±1.3	0.011
CoO	Co-O	6*	2.09±0.04	0.0137	-2.9±0.7	0.006
	Co-O-Co	12*	3.00±0.02	0.0102		
Co_3O_4	Co-O	4*	1.99±0.04	0.0056	7.9±1.9	0.017
	Co-O-Co	12*	3.47±0.01	0.0069		
Co-sample	Co-O	4.12±0.2	2.00±0.05	0.0047	-5.8±0.6	0.004

Note*: EXAFS fitting parameters at the Co K-edge for various samples (S_0^2=0.90). ^aCN: coordination numbers; ^bR: bond distance; $^c\sigma^2$: Debye-Waller factors; $^d\Delta E_0$: the inner potential correction. R factor: goodness of fit.

Just Accepted

Error bounds that characterize the structural parameters obtained by EXAFS spectroscopy were estimated as CN±20%, R ± 1%, σ^2 ± 20%.

Table S4. Formation rates of CO and CH_4 products from CO_2 photoreduction over typical Bi-based semiconductor photocatalysts.

Photocatalysts	Irradiation sources	CO (μmol h^{-1} g^{-1})	CH_4 (μmol h^{-1} g^{-1})	Refs.
Bi_2MoO_6/Co_3O_4	Xenon lamp (300W)	0	28.5	[3]
Bi_2MoO_6-OVs	Xenon lamp (300W: λ ≥ 420 nm)	0.27	2.04	[4]
Au/HMS-Bi_2MoO_6	Xenon lamp (300W: λ ≥ 420 nm)	2.3	37.6	[5]
Bi_2MoO_6 ultrathin nanosheets	Xenon lamp (300W)	3.62	-	[6]
$Bi_2MoO_6/Zn_3V_2O_8$	visible light	7.67	0.46	[7]
Bi_2MoO_6/BiOI	Xenon lamp (300W)	8.34	3.31	[8]
Bi_2MoO_6/BiO_{2-x}	Xenon lamp (300W)	16.36	-	[9]
$Bi_2MoO_6@ZnIn_2S_4$	visible light	23.11	2.26	[10]
Bi_2MoO_6/ln_2S_3	Xenon lamp (300W: λ ≥ 420 nm)	28.54	-	[11]
$TiO_2@Bi_2MoO_6$	Xenon lamp (300W: λ ≥ 420 nm)	30.66	-	[12]
3D Bi_2MoO_6 microspheres	Xenon lamp (300W)	41.5	-	[13]
Bi_2MoO_6/ACSs	Xenon lamp (300W)	58.03	-	[14]
CD/V_OR-Bi_2MoO_6	Xenon lamp (300W)	60.00	-	[15]
VOs-Bi_2MoO_6/MoS_xSe_y	Xenon lamp (300W)	60.58	8.65	[16]
Bi-α-MnS-Bi_2MoO_6	visible light (λ > 420 nm)	61.11	-	[17]
CeO_2/Bi_2MoO_6	Xenon lamp (300W: λ ≥ 420 nm)	65.3	2.46	[18]
Ni-MOF/Bi_2MoO_6	Xenon lamp (300W)	66.34	10.27	[19]
$ZnIn_2S_4/Bi_2WO_6$	Xenon lamp (300W)	0.5	5.12	[20]
CdS-Bi_2WO_6-S	Xenon lamp (300W:λ > 420 nm)	13.7	1.2	[21]
$Cs_2AgBiBr_6/Bi_2WO_6$	Xenon lamp (300W: λ = 400 nm)	42.19	0.41	[22]
$CeO_2/BiVO_4$	Xenon lamp (300W)	53	36	[23]
BiOBr/Bi_2WO_6	Xenon lamp (300W)	55.17	-	[24]
Co-Bi_2WO_6@Ce-MOF	Xenon lamp (300W)	77.1	11.4	[25]
NiO/BiOCl	Xenon lamp (300W)	78.11	2.31	[26]
Bi_2O_{3-x}/NiAl-LDH	Xenon lamp (300W)	83.55	-	[27]

Just Accepted

5%Co-Bi_2MoO_6	Xenon lamp (300W)	158.47	2.86	This work

References

[1] Kresse, G.; Furthmüller, J. Efficiency of ab-initio total energy calculations for metals and semiconductors using a plane-wave basis set. *Comp. Mater. Sci.* 1996, 6, 15–50.

[2] Hafner, J. Ab-initio simulations of materials using VASP: Density-functional theory and beyond. *J. Comput. Chem.* 2008, 29, 2044–2078.

[3] Fan, J. S.; Shi, L.; Ge, H. N.; Liu, J. C.; Deng, X. Z.; Li, Z. Y.; Liang, Q. Regulating the oxygen vacancy on Bi_2MoO_6/Co_3O_4 core‐shell nanocage enables highly selective CO_2 photoreduction to CH_4. *Adv. Funct. Mater.* 2025, 35, 2412078.

[4] Yang, X. L.; Wang, S. Y.; Yang, N.; Zhou, W.; Wang, P.; Jiang, K.; Li, S.; Ye, J. H. Oxygen vacancies induced special CO_2 adsorption modes on Bi_2MoO_6 for highly selective conversion to CH_4. *Appl. Catal. B: Environ.* 2019, 259, 118088.

[5] He, W. J.; Wei, Y. C.; Xiong, J.; Tang, Z. L.; Song, W. Y.; Liu, J.; Zhao, Z. Insight into reaction pathways of CO_2 photoreduction into CH_4 over hollow microsphere Bi_2MoO_6-supported Au catalysts. *Chem. Eng. J.* 2022, 433, 133540.

[6] Di, J.; Zhao, X. X.; Lian, C.; Ji, M. X.; Xia, J. X.; Xiong, J.; Zhou, W.; Cao, X. Z.; She, Y. B.; Liu, H. L.; et al. Atomically-thin Bi_2MoO_6 nanosheets with vacancy pairs for improved photocatalytic CO_2 reduction. *Nano Energy* 2019, 61, 54–59.

[7] Li, S. P.; Hasan, N.; Zhang, F. C.; Bae, J. S.; Liu, C. L. 2D $Bi_2MoO_6/Zn_3V_2O_8$ heterojunction photocatalyst for efficient photocatalytic reduction of CO_2 to CO and CH_4. *J. Colloid Interface Sci.* 2023, 652, 1533–1544.

[8] Wang, Z. L.; Cheng, B.; Zhang, L. Y.; Yu, J. G.; Li, Y. J.; Wageh, S.; Al-Ghamdi, A. A. S-scheme 2D/2D Bi_2MoO_6/BiOI van der Waals heterojunction for CO_2 photoreduction. *Chin. J. Catal.* 2022, 43, 1657–1666.

[9] Zhu, X. W.; Wang, Z. L.; Zhong, K.; Li, Q. D.; Ding, P. H.; Feng, Z. Y.; Yang, J. M.; Du, Y. S.; Song, Y. H.; Hua, Y. J.; et al. Mo-O-Bi Bonds as interfacial electron transport bridges to fuel CO_2 photoreduction via in-situ reconstruction of black Bi_2MoO_6/BiO_{2-x} heterojunction. *Chem. Eng. J.* 2022, 429, 132204.

[10] He, J. L.; Lin, J.; Zhang, Y.; Hu, Y. F.; Huang, Q. L.; Zhou, G. B.; Li, W.; Hu, J. Q.; Hu, N.; Yang, Z. Interfacial Mo-S bond-reinforced hierarchical S-scheme heterostructure of $Bi_2MoO_6@ZnIn_2S_4$ for highly-selective and efficient CO_2 photoreduction into CO. *Chem. Eng. J.* 2024, 480, 148036.

Just Accepted

[11] Yu, B.; Wu, Y. X.; Meng, F. M.; Wang, Q.; Jia, X. Q.; Khan, M. W.; Huang, C. M.; Zhang, S. Y.; Yang, L.; Wu, H. Formation of hierarchical Bi_2MoO_6/In_2S_3 S-scheme heterojunction with rich oxygen vacancies for boosting photocatalytic CO_2 reduction. *Chem. Eng. J.* 2022, 429, 132456.

[12] Ren, G. M.; Wei, Z. X.; Li, Z. Z.; Zhang, X. C.; Meng, X. C. Fabrication of S-scheme hollow $TiO_2@Bi_2MoO_6$ composite for efficiently photocatalytic CO_2 reduction. *Mater. Today Chem.* 2023, 27, 101260.

[13] Zhang, X. C.; Ren, G. M.; Zhang, C. M.; Li, R.; Zhao, Q.; Fan, C. M. Photocatalytic reduction of CO_2 to CO over 3D Bi_2MoO_6 microspheres: simple synthesis, high efficiency and selectivity, reaction mechanism. *Catal. Lett.* 2020, 150, 2510–2516.

[14] Zhang, X. C.; Ren, G. M.; Zhang, C. M.; Xue, J. B.; Zhao, Q.; Li, R.; Wang, Y. F.; Fan, C. M. Assisting Bi_2MoO_6 microspheres with phenolic resin-based ACSs as attractive tailor-made supporter for highly-efficient photocatalytic CO_2 reduction. *Green Energy Environ.* 2021, 6, 693–702.

[15] Lin, J.; He, J. L.; Huang, Q. L.; Luo, Y.; Zhang, Y.; Li, W.; Zhou, G. B.; Hu, J. Q.; Yang, Z.; Zhou, Y. Interfacial Bi-O-C bonds and rich oxygen vacancies synergistically endow carbon quantum dot/Bi_2MoO_6 with prominent photocatalytic CO_2 reduction into CO. *Appl. Catal. B: Environ. Energy* 2025, 362, 124747.

[16] Qian, G. L.; Li, J. X.; Tan, H. L.; Tang, L. Y.; Yu, X. L.; Li, W. T.; Ma, S. H.; Xie, Q.; Li, J.; Long, D. In-situ fabrication of oxygen vacancy rich S-scheme Bi_2MoO_6/MoS_xSe_y heterojunction for efficient CO_2 photoreduction with low-concentration. *Appl. Catal. B: Environ. Energy* 2026, 383, 126017.

[17] Liu, L. Z.; Dai, K.; Zhang, J. F.; Li, L. L. Plasmonic Bi-enhanced ammoniated α-MnS/Bi_2MoO_6 S-scheme heterostructure for visible-light-driven CO_2 reduction. *J. Colloid Interface Sci.* 2021, 604, 844–855.

[18] Xu, X. T.; Shao, C. F.; Zhang, J. F.; Wang, Z. L.; Dai, K. Rational design of S-scheme CeO_2/Bi_2MoO_6 microsphere heterojunction for efficient photocatalytic CO_2 reduction. *Acta Phys.-Chim. Sin.* 2024, 40, 2309031.

[19] Jiang, J. J.; Li, Y. R.; Zhang, F. J.; Wang, Y. R. Novel honeycomb-like Ni-MOF enhanced hierarchical Bi_2MoO_6 microspheres for high efficient photocatalytic CO_2 reduction. *Inorg. Chem. Commun.* 2023, 156, 111271.

[20] Yang, W.; Zhou, F. H.; Sun, N. C.; Wu, J.; Qi, Y. F.; Zhang, Y. L.; Song, J. Y.; Sun, Y. J.; Liu, Q. Z.; Wang, X. D.; et al. Constructing a 3D $Bi_2WO_6/ZnIn_2S_4$ direct Z-scheme heterostructure for improved photocatalytic CO_2 reduction performance. *J. Colloid Interface Sci.* 2024, 662, 695–706.

[21] Hao, M. M.; Wei, D. Q.; Li, Z. H. Rational design of an efficient S-scheme heterojunction of

Just Accepted

CdS/Bi_2WO_6–S nanocomposites for photocatalytic CO_2 reduction. *Energy Fuels* 2022, 36, 11524–11531.

[22] Wu, L. J.; Zheng, S.; Lin, H.; Zhou, S.; Idris, A. M.; Wang, J.; Li, S.; Li, Z. Q. In-situ assembling 0D/2D Z-scheme heterojunction of lead-free $Cs_2AgBiBr_6/Bi_2WO_6$ for enhanced photocatalytic CO_2 reduction. *J. Colloid Interface Sci.* 2023, 629, 233–242.

[23] Geng, J. G.; Guo, S. X.; Zou, Z. Y.; Yuan, Z. Z.; Zhang, D.; Yan, X. T.; Ning, X. F.; Fan, X. J. 0D/2D $CeO_2/BiVO_4$ S-scheme photocatalyst for production of solar fuels from CO_2. *Fuel* 2023, 333, 126417.

[24] Wu, J. M.; Li, K. Y.; Yang, S. Y.; Song, C. S.; Guo, X. W. In-situ construction of $BiOBr/Bi_2WO_6$ S-scheme heterojunction nanoflowers for highly efficient CO_2 photoreduction: Regulation of morphology and surface oxygen vacancy. *Chem. Eng. J.* 2023, 452, 139493.

[25] Ren, J. L.; Ma, Q. F.; Sun, X. F.; Wang, S. F.; Liu, G. R.; Yang, H. Interface-engineering enhanced photocatalytic conversion of CO_2 into solar fuels over S-type $Co\text{-}Bi_2WO_6$@Ce-MOF heterostructured photocatalysts. *J. Colloid Interface Sci.* 2025, 691, 137452.

[26] Wang, K.; Sun, T.; Ma, H.; Wang, Y.; He, Z. H.; Wang, H.; Wang, W. T.; Yang, Y. Y.; Wang, L.; Liu, Z. T. Energy band modulating of NiO/BiOCl heterojunction with transition from type-II to S-scheme for enhancing photocatalytic CO_2 reduction. *Chem. Eng. J.* 2024, 480, 154711.

[27] Han, H. R.; Zhang, S. B.; Song, S. S.; Zhang, W. J.; Liu, D. D.; Song, Z. H.; Wang, Q. Y.; Ma, C. C.; Feng, S.; Duan, X. M. Construction of Bi_2O_{3-x}/NiAl-LDH S-scheme heterojunction for boosting photothermal-assisted photocatalytic CO_2 reduction. *Appl. Surf. Sci.* 2024, 662, 160122.

Just Accepted